Title

A 200-year snapshot of soil development in pyroclastic deposits derived from the 1815 super explosive eruption of Mount Tambora in Indonesia

Permalink

https://escholarship.org/uc/item/2g80k44n

Authors

Anda, Markus
Purwanto, Setiyo
Dariah, Ai
et al.

Publication Date

2023-05-01

DOI

10.1016/j.geoderma.2023.116454

Peer reviewed

A 200-year snapshot of soil development in pyroclastic deposits derived from the 1815 super explosive eruption of Mount Tambora in Indonesia

Markus Anda [a,1,*], Setiyo Purwanto [b], Ai Dariah [c,1], Tetsuhiro Watanabe [d], Randy A. Dahlgren [e]

[a] Research Centre for Geospatial, National Research and Innovation Agency, Jalan Raya Jakarta-Bogor Km 46 Cibinong, Bogor 16911, Indonesia
[b] Indonesian Center for Agricultural Land Resource Research and Development, Agency of Agricultural, Research and Development, Jalan Tentara Pelajar No.12, Kampus Penelitian Pertanian, Cimanggu, Bogor 16114, Indonesia
[c] Research Center for Horticultural and Estate Crops, National Research and Innovation Agency, Jl. Raya Jakarta-Bogor Km 46, Cibinong Bogor 16911, West Java, Indonesia
[d] Graduate School of Agriculture, Kyoto University, Kyoto 606-8502, Japan
[e] Department of Land, Air and Water Resources, University of California Davis, Davis 95616, CA, USA

ARTICLE INFO

ABSTRACT

Early-stage pedogenic processes and formation rates on completely obliterated volcanic landscapes, such as the super explosive 1815 Mount Tambora eruption, have not previously been robustly explored. The objectives of this study were to determine (i) the mineralogical composition of the sand fraction, selected physical and chemical soil properties and potential nutrient reserves after 200 years of pedogenesis, and (ii) chemical weathering indices, rate of soil formation, and rates of C and N accretion. Soil formation was examined for five soil profiles on stable plain/foot slope positions representing the diversity of soils in these landscape positions, which are important for agricultural production. Results showed that the soil mineralogical composition of the sand fraction was dominated by easily weatherable minerals (e.g., labradorite and augite volcanic glass) indicating high potential nutrient reserves (e.g., Ca^{2+}, Mg^{2+}, K^+, P) as confirmed by X-ray fluorescence (XRF) analyses. Allophanic material formation was minimal ($<2.3\%$) owing to the preferential accumulation of Al^{3+} into Al-humic complexes. The low contents of allophanic materials and metal-humus complexes resulted in low P-retention (17.5–43.4%) within the soil solum, with the highest value in surface horizons (33–43%). Morphological features showed rapid solum (A + B horizons) development of 22 to 107 cm. Shallow soils occurred on shallow eruption deposits (consisting of pyroclastic flow underlain by pumice), whereas the deepest soils were found on thick deposit consisting of either trachyandesite pyroclastic or basaltic andesite materials. The chemical index of alteration (CIA) followed the order of A horizons (48.4 ± 4.6) > B horizons (45.4 ± 2.4) > C horizons (43.8 ± 4.2) $\approx$ tephra/lava (43.1), indicating accumulation of Al oxides and depletion of base cations in the upper horizons. Similarly, the base depletion index (BDI) showed a trend of A horizons (1.13 ± 0.18) < B horizons (1.25 ± 0.09) < C horizons (1.34 ± 0.20) $\approx$ tephra/lava (1.35), indicating depletion of base cations (Ca^{2+}, Mg^{2+}, K^+, Na^+) from the soil surface to C horizons. Based on solum depths (A + B horizons) and 200 years of post-eruption soil development, the solum formation rate ranged from 1.2 to 5.3 mm yr^{-1}. Appreciable stocks of SOC (2.3–12.8 kg C m^{-2}) and SON (0.21–0.77 kg m^{-2}) accumulated over the 200 year period. Eruption materials from the Mt. Tambora eruption with a precisely known timescale contributed new pedological insights documenting rapid soil formation rates from pyroclastic materials leading to a rapid recovery of soil functions to support agricultural production.

* Corresponding author at: Research Center for Geospatial, National Research and Innovation Agency, Jalan Raya Jakarta-Bogor Km 46 Cibinong, Bogor 16911, West Java, Indonesia.
E-mail address: markusandas@yahoo.com (M. Anda).
[1] Previous address: Indonesian Center for Agricultural Land Resource Research and Development, Agency of Agricultural Research and Development, Jalan Tentara Pelajar No.12, Kampus.

1. Introduction

Volcanoes are revered and feared for their awesome and devastating eruptions that can obliterate terrestrial ecosystems. Yet from these ashes of devastation arise some of the most productive soils in the world with the capacity to sustain high human population densities (Dahlgren et al., 2004). The 1815 eruption of Tambora, the most powerful volcanic eruption in recorded human history (e.g. Yokoyama, 1957; Self et al., 1984), provides an excellent opportunity to examine soil mineralogy, the early stage of pedogenesis and the physical and chemical properties of Andisols on the rejuvenating landscapes. Given the high population density surrounding many tropical volcanoes and the frequent occurrence of eruptions, it is critical to assess the recovery time of landscapes for agricultural production to sustain indigenous populations.

Tambora volcano erupted in April 1815 on Sumbawa Island, Indonesia and is the only eruption to be rated at the volcanic explosivity index of magnitude 7 (values range from 0 = gentle to 8 = mega-colossal eruption) in modern history (Gertisser and Self, 2015). The 1815 eruption produced 175 km^3 of volcanic ejecta (Self et al., 1984) consisting of ~ 150 km^3 ash and ~ 25 km^3 ignimbrite (Stothers, 1984). The dust/ash entering the upper atmosphere (~40 km^3) and sulfate aerosols injected into the stratosphere caused a global cooling event lasting for three years (Self et al., 2004) and is noted for causing the 1816 year-without-summer in the northern hemisphere that led to widespread crop failures (Stommel and Stommel, 1979; Stothers, 1984; van Oosterzee 1997).

In spite of the vast literature on soils formed in volcanic deposits, little is known about early-stage pedogenic processes and rates on completely obliterated volcanic landscapes, especially in tropical regions. Chemical weathering is considered rapid in volcanic ejecta owing to its high surface area and porosity, along with the glassy nature of the material (Dahlgren et al., 1999). In terms of agricultural productivity, the initial volcanic deposits are abundant in rock-derived nutrients owing to the high rates of chemical weathering, but are distinctly deficient in nitrogen, which must accumulate by nitrogen fixation during primary succession of vegetation communities. For the Mt. Shasta mudflow sequence in northern California, organic matter accumulation (C and N stocks) reached an approximate steady-state after ~ 250 years (Dickson and Crocker, 1953, 1954; Sollins et al., 1983) in the temperate climate. Furthermore, water and nutrient holding capacities are generally low in recent volcanic deposits due to their low clay and organic matter concentrations. As weathering proceeds, the accumulation of short-range-order materials (e.g., allophane, imogolite, ferrihydrite) and Al/Fe-humus complexes leads to high P-retention and the potential for P deficiency. Overall, agricultural productivity in volcanic deposits increases as weathering/pedogenesis initially proceeds, reaches a maximum in moderately weathered soils, although high P-retention can be a problem, and then declines in more highly weathered soils as soil acidity and potential Al toxicity become more acute, and the supply of rock-derived nutrients becomes depleted by chemical weathering/leaching. The timing for this progression in agricultural productivity strongly depends on the climatic regime (Dahlgren et al., 2004).

The characteristics of volcanic materials erupted from Tambora in 1815 have been well documented (e.g., Stothers, 1984; Sigurdsson and Carey, 1989; Self et al., 1984); however, post-eruption soil characteristics and developmental processes have not yet been explored. The precise timing of the Tambora eruption allows an assessment of 202 years (1815–2017, hereafter rounded to 200 yr) of soil development on rejuvenating landscapes in a tropical climate. In addition, the evaluation of nutrient reserves in weatherable minerals of eruption materials from Tambora is crucial for soil fertility management, but has not yet been evaluated. The primary objectives of this study were to determine (i) the mineralogical composition of sand fraction, soil properties and potential nutrient reserves after 200 years of pedogenesis, and (ii) chemical weathering indices, rate of soil formation, and rates of C and N accretion. The assessment of soil mineralogy, chemical weathering/alterations and soil chemical properties provides new information for understanding the potential nutrient reserves in weatherable minerals, the early stages and rates of soil formation on volcanic materials under tropical conditions and the recovery time of these devastated landscape to sustain agricultural production.

2. Materials and methods

2.1. Soil forming environment and field sampling

The study area is located on the northern portion of Sumbawa Island, Indonesia and lies between 8°10'−8°30' S latitude and 117°40'–118°10' E longitude, with elevations ranging from 27 to 157 m above mean sea level (Fig. 1). Climate is tropical monsoon with a rainy season from December to March and a distinct dry season from June to September (Fig. S1). Mean annual temperature and precipitation at nearby Sumbawa-Besar (40 km southwest of Mt. Tambora) are 27.5 °C and 1370 mm, respectively. Climatic data estimates for each of the five sites were obtained from the WorldClim database (Fig. S1; Fick and Hijmans, 2017). The soil temperature regime is isohyperthermic, and the soil moisture regime is ustic owing to the distinct dry period.

Study sites were selected on volcanic plain/footslope positions (slope = 5–8 %), as these landforms were considered representing the topographic positions with maximum soil development and the highest agricultural value. Based on an extensive field investigation, the five soils selected for intensive investigation were deemed representative of the overall diversity of soils formed on volcanic plain/footslope positions in the vicinity of Tambora. Considerable variability in soil depth occurred across our sampling sites, such as the eastern and southern locations having finer/deeper materials (up to 130 cm), whereas the western locations had moderately thick (60 cm) deposits derived from interbedded tephra and coarse pumice (Table 1). The 1815 eruption obliterated the native vegetation resulting in primary succession from barren surfaces. Current vegetation at the study sites was savanna-grasslands (rangelands) with some bidara (*Ziziphus mauritiana*) trees for SWS15, SWS16 and SWS17, cashew nut (*Anacardium occidentale*) and shrubs for SWS11, and upland food crops (e.g., maize, banana and fruits) for SWS2 (Figs. S2 and S3).

According to Sudradjat et al. (1998) the lithology of the sampling sites consisted of lava breccia with andesitic lava, lahar, tuff and volcanic ash constituents. These materials consisted of hornblende andesite and hornblende-augite-biotite andesite (Sudradjat et al., 1998). Field observation of the parent materials for the studied soil profiles are shown in Figs. 2 and 3. The SWS2 profile developed from a pyroclastic flow of vesicular trachyandesite (Fig. 2a) overlying interlayered ashfall and pumice (Fig. 2b). The SWS11 profile developed from basaltic-andesite with whitish phenocrysts (Fig. 2c). Profiles SWS15, SWS16 and SWS17 had parent materials derived from vesicular trachyandesite and breccia (Fig. 3). The fresh surfaces of vesicular trachyandesite and breccia were exposed on the soil surface as shown in Fig. 3a and Fig. 3b, respectively. The exposed internal surface (following breaking with a geological hammer) of trachyandesite showed a dark color and vesicular texture (Fig. 3c), whereas weathered trachyandesite collected from soil pits showed vesicular texture and reddish color with surfaces coated by a reddish weathering product (Fig. 3d).

We excavated a soil pit to the depth of the interface with the underlying paleosol or the C horizon of modern soils (dimensions of 150 × 200 × 110–133 cm (width × length × depth), described soil morphological properties and collected a composite sample for each soil horizon from all sides of the evacuated pit (Figs. 4 and 5). The sample was thoroughly mixed prior to subsampling ~ 1 kg for analysis. Soils were air dried, gently crushed, and passed through a 2-mm sieve to remove coarse fragments and visible roots prior to laboratory analysis. We also collected fresh trachyandesite and weathered vesicular trachyandesite on the surface and within the profile of SWS17 site; and a fresh boulder of basaltic andesite lava at the SWS11 site for
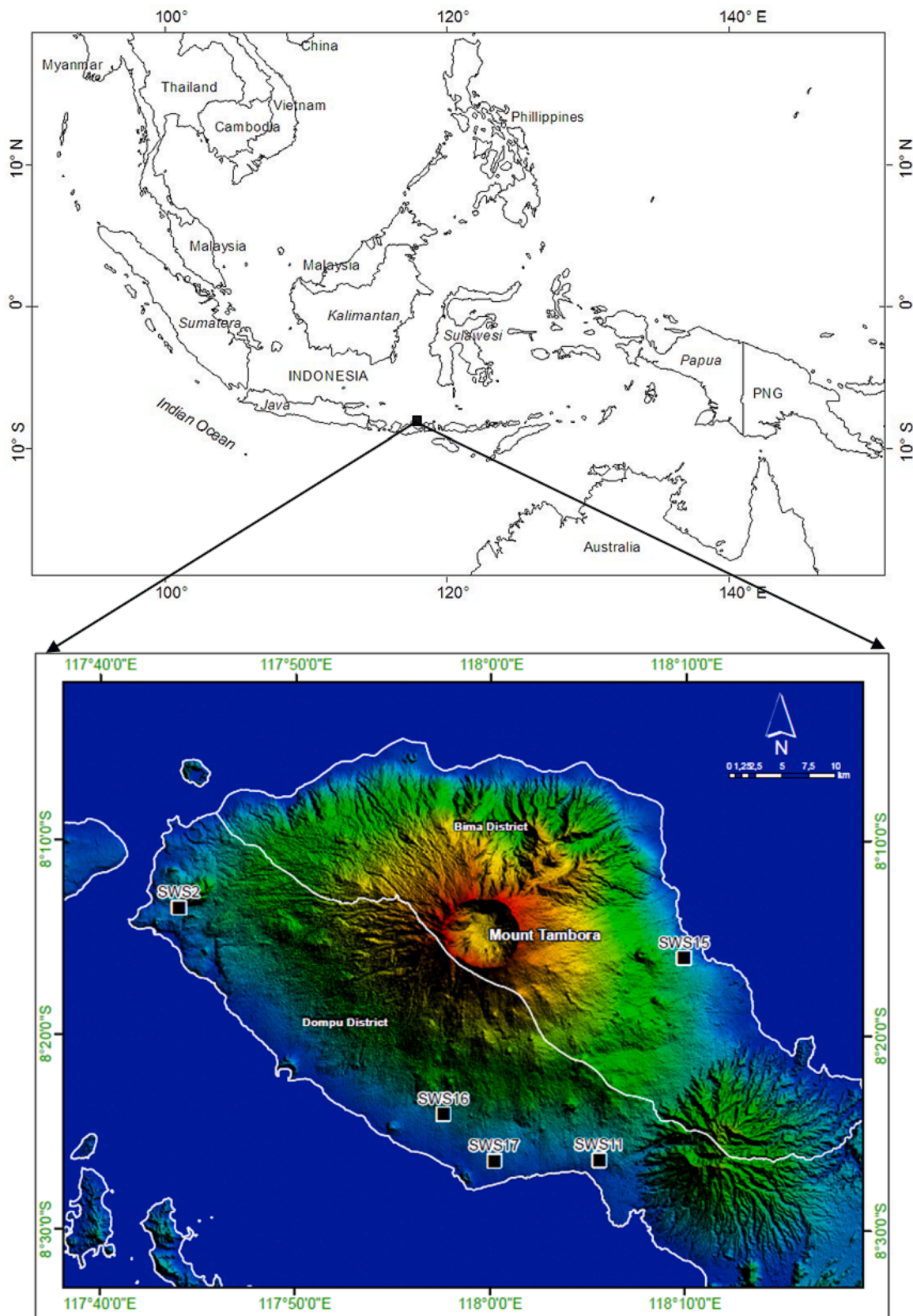
Fig. 1. Study area and soil sampling locations (solid square) surrounding Mt. Tambora.

Table 1
Morphological description of soil profiles derived from the 1815 eruption of Mt. Tambora.

Profile/ Horizon	Depth	Matrix color	Field texture	Structure	Consistency (moist)	Roots	Gravel	Horizon boundary	Texture modifier
	cm						%		
SWS2 Typic Ustivitrand (93 m asl)									
Ap	0–22/27	7.5YR 5/4	SiL	w m g	ns and np	m f	–	a w	–
C1	22/27–43/45	7.5YR 4/1	S (pumice)	loose	ns and np	fw f	30	a w	g s p
C2	43/45–45/50	10 YR 6/2	Si (ashfall)	massive	ns and np	–	–	a w	vf af
C3	45/50–52/54	7.5YR 4/1	S (pumice)	loose	ns and np	–	30	a w	g s p
C4	52/54–57	10 YR 6/2	Si (ashfall)	massive	ns and np	–	–	a w	vf af
2Ab1	57–83	7.5YR 4/4	CL	m m sb	s and p	–	–	g s	–
2Bb2	83–125	7.5YR 4/4	CL	m m sb	s and p	–	–	–	–
SWS16 Dystric Vitric Haplustand (157 m asl)									
A	0–15	7.5YR 4/2	SL	w f g	ns and np	m f	5	g s	sl g SL
Bw1	15–39/53	7.5YR 4/2	SL	w f g	ns and np	m f	13	d w	g SL
Bw2	39/53–78	2.5 YR 3/3	SL	w f g	ns and np	c f	8	d s	sl g SL
Bw3/C1	78–97	2.5YR 4/4	SL	w f g	ns and np	c f	25	d s	g SL
Bw4/C2	97–130	2.5YR 4/4	SL	w f g	ns and np	c f	32	d s	g SL
SWS17 Dystric Vitric Haplustand (32 m asl)									
A	0–20	7.5YR 3/2	SL	w f g	ns and np	m f	27	c s	g SL
Bw1	20–55	5YR 4/2	SL	w f g	ns and np	m f	33	c s	g SL
Bw2/C1	55–85	5YR 4/4	SL	w f g	ns and np	c f	25	g s	g SL
Bw3/C2	85–100	2.5YR 4/4	SL	w f g	ns and np	c f	25	d s	g SL
Bw4/C3	100–130	2.5YR 4/6	SL	w f g	ns and np	fw f	25	–	g SL
SWS11 Dystric Vitric Haplustand (27 m asl)									
A	0–30	10YR 3/1	SL	w f g	ns and np	m f	5	c s	sl g SL
Bw1	30–62	5YR 5/6	SL	w f g	ns and np	fw f	22	d s	g SL
Bw2/C1	62–97	5YR 5/6	SL	w f g	ns and np	–	25	d s	g SL
Bw3/C2	97–110	5YR 5/6	SL	w f g	ns and np	–	25	–	g SL
SWS15 Dystric Vitric Haplustand (48 m asl)									
A	0–20	10YR 3/1	SL	massive	ns and np	m f	–	g s	–
Bw	20–37/42	10YR 4/2	SL	w f g	ns and np	fw f	–	a w	–
C1	37/42–55	10 YR 4/3	coarse S	loose	ns and np	–	–	a s	–
C2	55–72	10 YR 4/3	fine S	loose	ns and np	–	–	a s	–
C3	72–81	7.5YR 4/3	SiL	massive	ns and np	–	–	a s	–
C4	81–89	10YR4/2	coarse S	loose	ns and np	–	–	a s	–
C5	89–99	10YR4/3	SiL	massive	ns and np	–	–	a s	–
C6	99–133	10YR4/1	coarse S	loose	ns and np	–	25	–	g SL

Notes: Consistence: ns = non-sticky, np = non-plastic, s = sticky, p = plastic.
Structure: w = weak, f = fine, m = medium, g = granular; m m sb = medium moderate subangular blocky.
Texture modifier: g s p = gravelly pumice sand, vf af = very fine ashfall, g SL = gravelly sandy loam,
sl g SL = slightly gravelly sandy loam.
Horizon boundary: a s = abrupt smooth, g s = gradual smooth, d s = diffuse smooth, a w = abrupt wavy;
Root: m = many, c = common, fw = few, f = fine.

mineralogical and elemental analyses. Soil characterization methods followed Soil Survey Staff (2014) standard methodologies unless otherwise noted.

The solum thickness (A + B horizons) is required to calculate the rate of soil formation and is expressed in mm/year. Solum thickness was determined by subtracting the C horizon component (volume basis) from mixed B/C horizons and then summing up all the A and B horizon thicknesses of the soil profile (equation (1).

$$H = \sum_{i}^{n} Si - (X*Si) \tag{1}$$

where H = total solum thickness of the profile (cm); Si = thickness of a given layer of the profile (cm); and X = fraction of C horizon (% volume).

2.2. Soil analyses

Soil bulk density (BD) of the fine-earth fraction (<2 mm) was measured by the core method using steel cylinders (7.3 × 4 cm; diameter × length). Bulk density was corrected for coarse fragments (>2 mm) and expressed on an oven-dry weight basis (García-Rodeja et al., 2004). Particle size of the fine-earth fraction was determined following pretreatment with H_2O_2 to remove organic matter and dispersion with dilute Na-hexametaphosphate. The clay- (<2 μm) and silt-size (2–50 μm) fractions were measured by the pipette method and the

sand fractions by wet sieving (Soil Survey Staff, 1992); the sand fraction was collected for subsequent mineralogical identification.

Soil pH was measured 1:5 (solid:solution) in H_2O and 1.0 M KCl. Electrical conductivity (25 °C) was determined on a 1:5 (solid:solution) in H_2O using a conductivity meter. Phosphate retention was determined according to Blakemore et al. (1987), and available phosphorus was estimated via bicarbonate extraction (Olsen 1954). Potential soil P and K fractions were assessed by extraction in 25% HCl. Exchangeable cations were displaced by 1 M NH_4OAc at pH 7.0, then the cations were measured in the supernatant (Soil Survey Staff, 1992) using atomic absorption spectroscopy. Cation exchange capacity (CEC) was determined in 1 M NH_4OAc (buffered at pH 7.0) after extraction of NH_4^+ by 10% NaCl. Base saturation was calculated as the sum of base cations extracted by 1 M NH_4OAc divided by CEC. Total C concentrations were determined using Walkley–Black wet oxidation (Soil Survey Staff, 1992) and total N by the Kjeldahl method (Bremner and Mulvaney, 1982). Soil C and N stocks (kg m^{-2}) were calculated by summing the masses contained in each soil horizon to a depth of 100 cm (or 57 cm in the case of the modern soil at SWS2): $\sum$ (SOC/SON × BD × D × [1 − CF], where SOC and SON are soil organic C and N contents, BD is bulk density, D is horizon depth and CF is coarse fragment fraction (>2-mm).

We used non-sequential selective dissolution in Na pyrophosphate, ammonium-oxalate and citrate-dithionite to characterize Fe, Al, Mn and Si in various pedogenic pools. The Fe, Al and C associated with metal-humus complexes (Al_p, Fe_p and C_p) were extracted with Na-
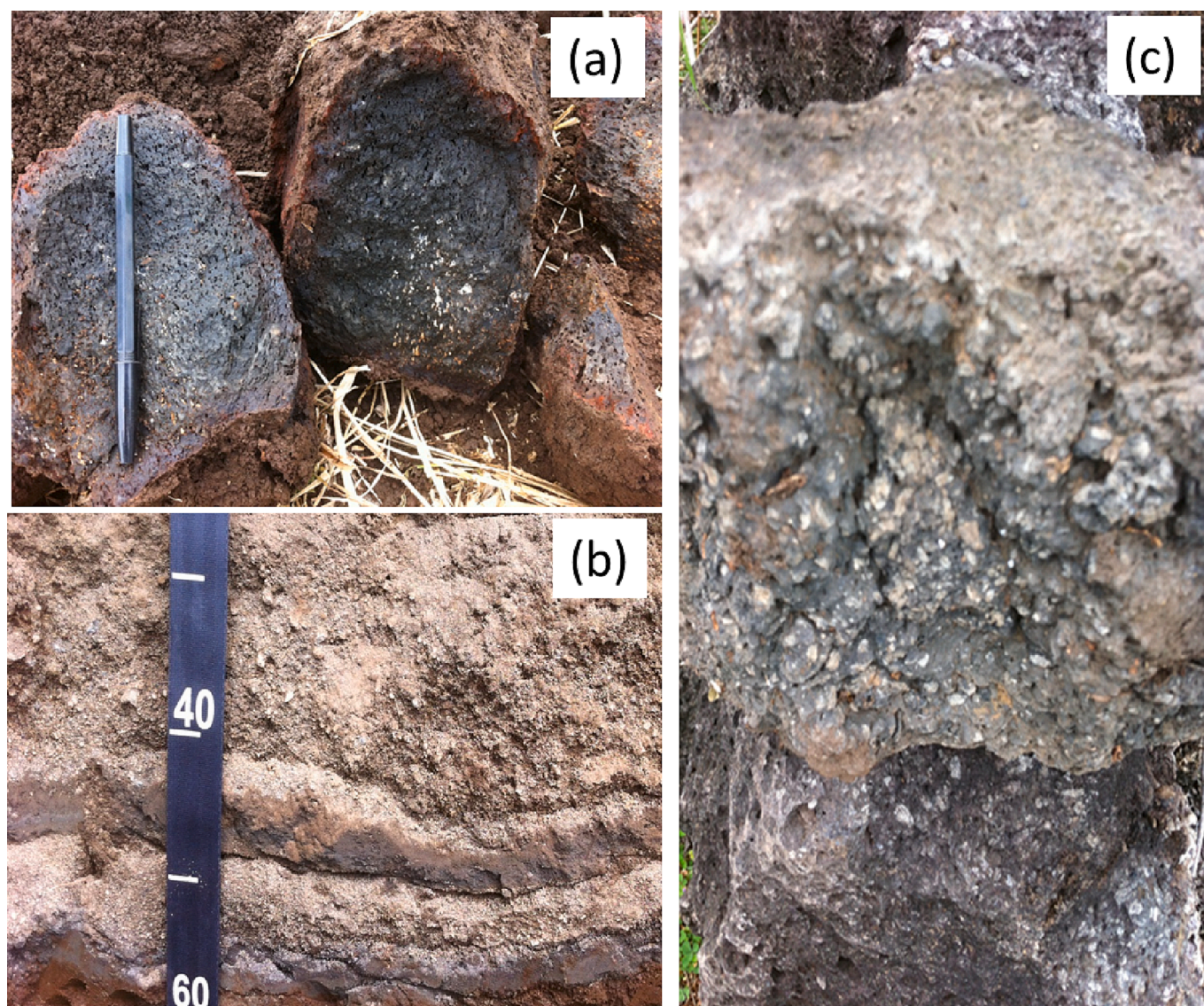
Fig. 2. Lithology consisted of pyroclastic flow/surge deposits and basaltic-andesite from the Tambora eruption as soil parent materials: (a) Vesicular trachyandesite overlying the interlayered ashfall and pumice shows the weathered outer surface and the exposed fresh internal surface (parent material of SWS2 profile), (b) interbedding ashfall and pumice underlain by a paleosol with reddish brown color, and (c) basaltic-andesite with whitish phenocrysts as parent material of the SWS11 profile. The pen is 14 cm as a scale.

pyrophosphate (Blakemore et al., 1987). Ammonium-oxalate extracted Al, Fe and Si (Al_o, Fe_o, and Si_o) from organic complexes, short-range-order (SRO) Fe-(hydr)oxides (e.g., ferrihydrite) and SRO aluminosilicates (e.g., allophane and imogolite; hereafter termed allophanic materials) (Soil Survey Staff 2014). Citrate-dithionite extraction (Fe_d, Mn_d) removed Fe and Mn from organic complexes and nanocrystalline-to-crystalline Fe/Mn-(hydr)oxide pools (Holmgren, 1967). All extracts were treated with 'Superfloc' and centrifuged before quantification of Fe, Al, Mn and Si by ICP-AES. The C_p concentration was quantified by Walkley–Black wet oxidation. Ferrihydrite concentration was calculated as $1.7 \times Fe_o$ (Parfitt and Childs, 1988) and allophane content according to Parfitt (1990): Allophane % = A $\times$ Si_o% (the A factor varied from 5 to 16 depending on (Al_o-Al_p):Si_o ratio; A = 5 at a 1:1 ratio and 16 for a 3.5:1 ratio or higher).

The mineralogical composition of the 50–250 μm sand fraction was identified using a polarizing microscope (Carl Zeiss, Germany). We counted a total of 300 grains using line count transects. Minerals were viewed using plain polarized light (PPL) and cross-polarized light (XPL) and identified according to Milner (1962). Mineral optical properties of

pleochroism under PPL and interference color under XPL were applied to distinguish anisotropic and isotropic minerals and their identification. Isotopic minerals appeared dark, while the anisotropic minerals have interference color when viewed under XPL. The glassy aggregates referred to sand fragments containing several minerals enclosed in a glassy matrix as observed under a polarized microscope.

2.3. Indices of chemical weathering

Total elemental analysis of soils and parent materials was determined using X-ray fluorescence (XRF). Samples were finely ground (<100 μm) using a ball mill and analyses were carried out on pressed pellets as described by Norrish and Chappell (1977). The powdered sample was mixed with carboxyl methyl cellulose as a binder and pressed into pellets using a boric acid backing in a stainless steel ring and subsequent oven drying at 55 °C for 30 min. A XRF (Thermo Scientific ARL 9900 Series, Germany) with a Be tube and scintillation counter was used to determine elemental composition at 60 kV/40 mA for Ba, Rb, Zr, Pb, Zr and; 40 kV/60 mA for Ni, Cu, Co, Si, Al, Fe, Mn, V, Cr, Ti, Ca, K;
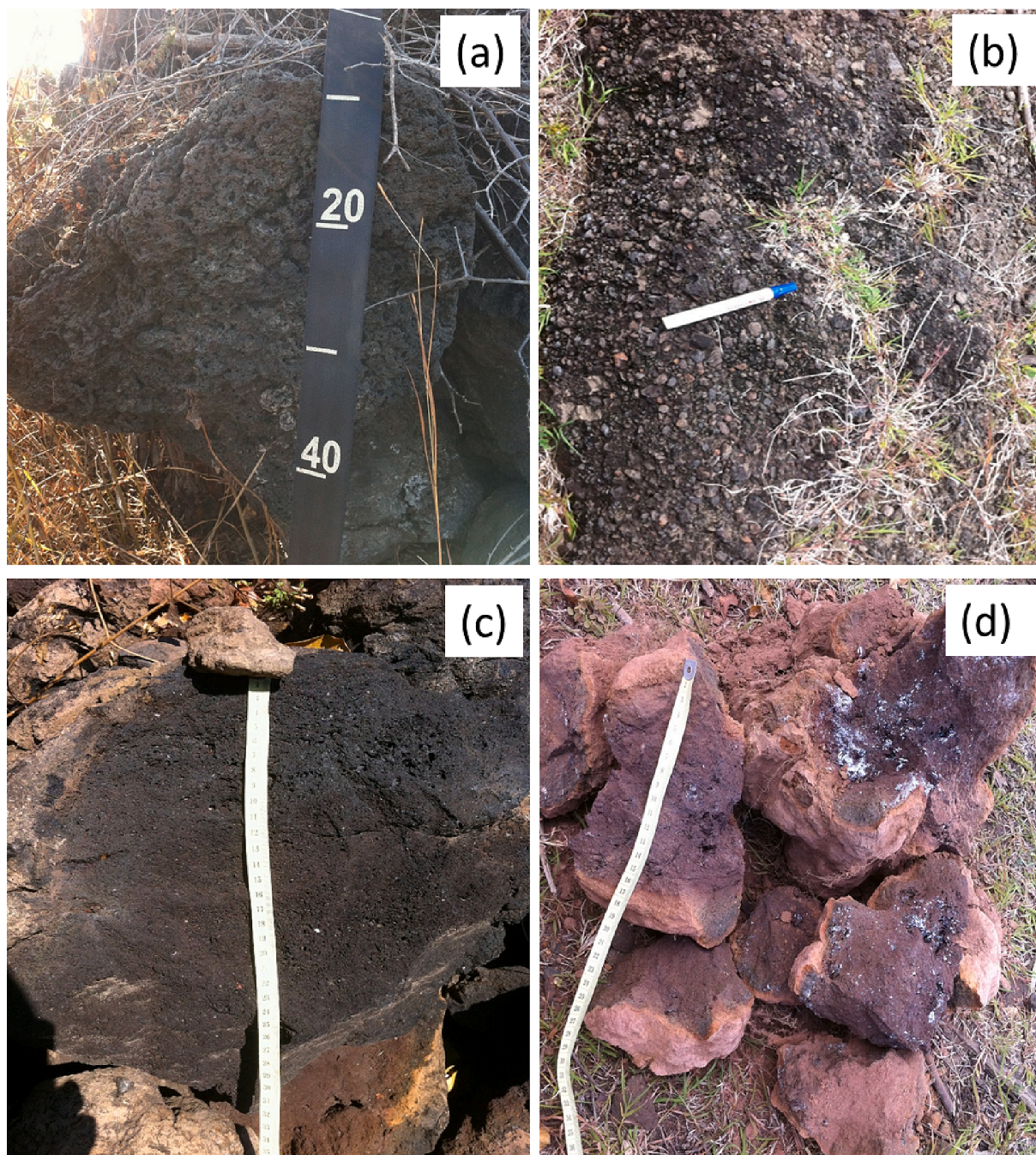
Fig. 3. Lithology consisted of pyroclastic flow deposits from the Tambora eruption as parent materials of SWS15, SWS16 and SWS17 profiles: (a) Unweathered vesicular trachyandesite exposed on the soil surface, (b) Unweathered pyroclastic flow-breccia with trachyandesite composition is exposed on the soil surface, (c) Exposed internal surface of trachyandesite showing the vesicular texture, and (d) Reddish colour of weathered trachyandesite collected from soil pit of SWS17. The pen marker is 14 cm as a scale.

and 30 kV/80 mA for Mg and Na. The content of each element is expressed on an oxide basis.

Chemical weathering was assessed using four metrics (Jien et al., 2016; Harnois, 1988; Nesbitt and Young, 1989). The chemical index of alteration (CIA) was calculated for soils, which uses oxide values converted to molar values calculated as: $CIA = [Al_2O_3/(Al_2O_3 + Na_2O + CaO + K_2O)] \times 100$. For reference, weathering products such as kaolinite have CIA values ~ 100, unaltered albite and potassium feldspars have CIA values ~ 50, and fresh basalts and granites have CIA values between 30 and 45 and 45–55 (Nesbitt and Young, 1982). Further, we calculated the base depletion index (BDI) = $(CaO + MgO + Na_2O + K_2O)/(Fe_2O_3 + Al_2O_3 + TiO_2)$. Finally, we

determined two desilication indices (DSI): $DSI-R1 = SiO_2 /Al_2O_3$ and $DSI-R2 = SiO_2/(Fe_2O_3 + Al_2O_3)$.

3. Results

3.1. Soil morphological features

Soils formed in deposits from the 1815 eruption of Mt. Tambora showed sharply contrasting morphological features. On the western flank of the volcano (profile SWS2; ~ 25 km from vent), new soil materials (hereafter referred to as modern soils) showed an abrupt boundary with the underlying paleosol at 57 cm (Table 1; Fig. S2b). Radiocarbon
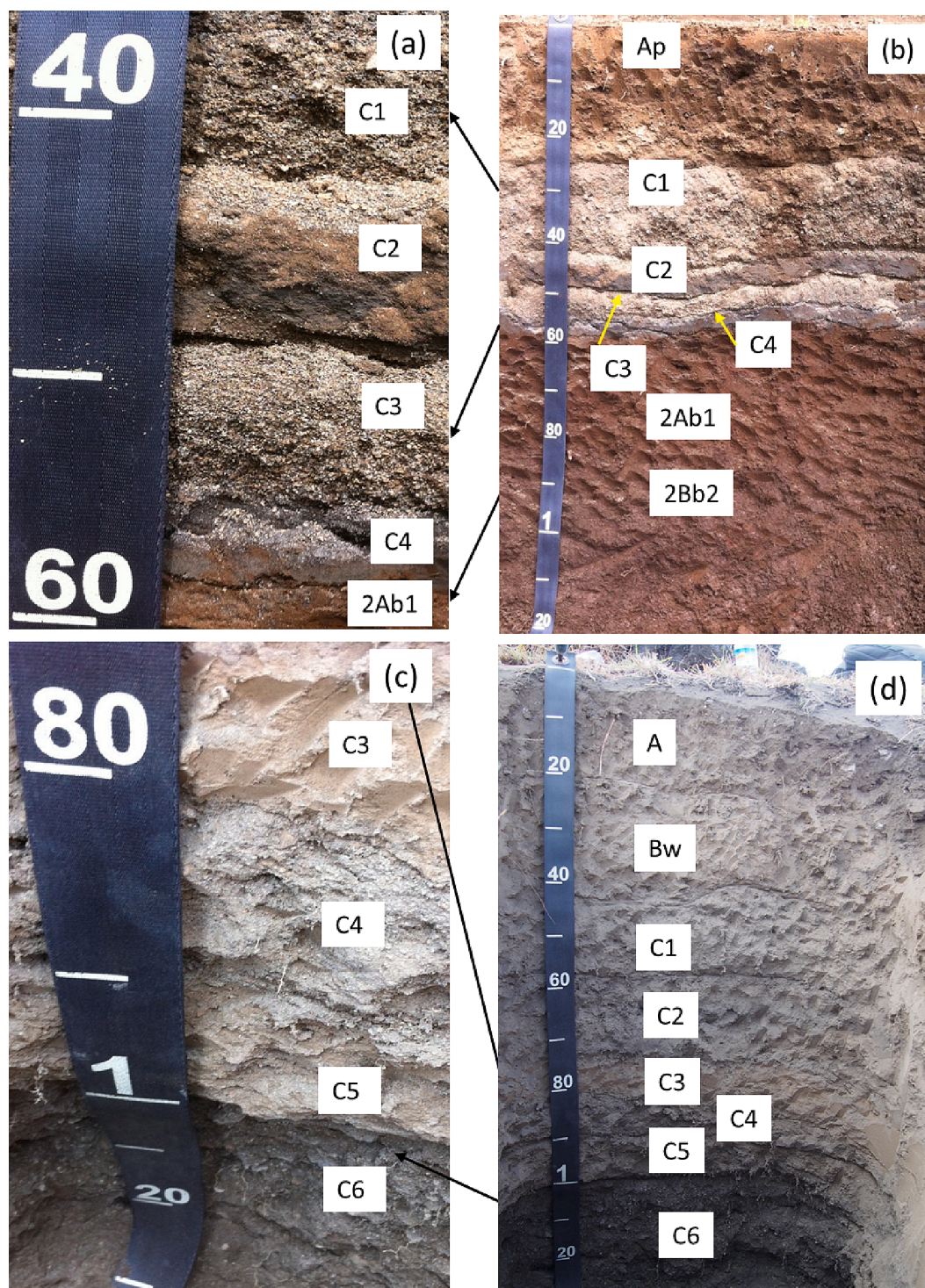
Fig. 4. Photographs of morphological features of the soil profile in the western and eastern flanks of Tambora: (a) Close-up of alternating pumice and fine ashfall deposits underlain the Ap horizon of SWS2 profile, (b) SWS2 profile showed brown topsoil with alternating pumice and fine ashfall deposits which in turn were underlain by a reddish-brown paleosol at 57 cm, (c) Close-up of alternating pyroclastic gravely, coarse sand and fine ashfall within SWS15 profile, and (d) SWS15 profile showing dark grey A and Bw horizons with alternating pyroclastic gravely, coarse sand and fine ashfall (C1-C6 layers). The paleosol was not present in SWS15 profile.

ages from the lower and upper portions of the Brown Tuff formation underlying the SWS2 profile suggest that the paleosol formed in deposits from intermittent volcanic activity between 5900 and 1210 ^{14}C years BP (Sigurdsson and Carey, 1992). The modern soil has an Ap horizon (22–27 cm thick) with brown color and silt loam texture overlying C horizons consisting of alternating dark-gray sandy pumice and light-brownish-gray, fine tephra deposits. In contrast, the underlying

paleosol horizons (2Ab1/2Bb2) were reddish brown with a clay loam texture and strong subangular blocky structure.

On the eastern flank (~15 km from vent), profile SWS15 had A/Bw horizon development with darker colors (values 3–4; chroma 1–2) and a sandy loam texture. The parent materials, C1–C6 horizons (37/42–133 cm depth), showed abrupt boundaries with alternating sandy lapilli and fine tephra deposits (Fig. 4). The underlying paleosol was not
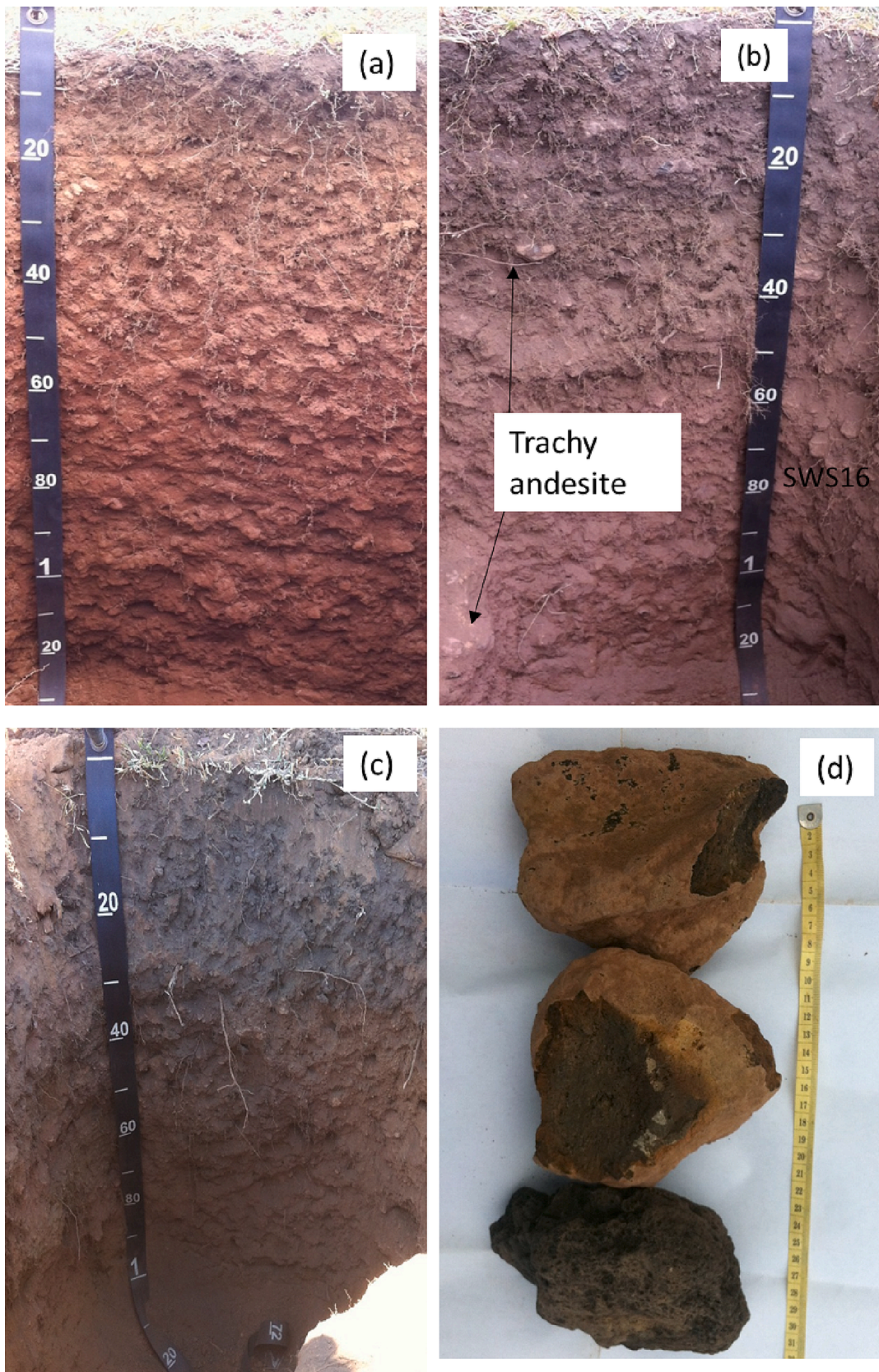
Fig. 5. Photographs showing morphological features of soil profiles and fine-root distribution to a depth of about 70 cm. Profiles show intense reddish color from rapid weathering: (a) SWS16 and (b) SWS17 profiles both developed from pyroclastic trachyandesite, c) SWS11 profile developed from basaltic-andesite, and (d) Weathered trachyandesite collected from upper profile of SWS17 compared to the bottom rock obtained at the soil surface.

reached within the 133 cm profile depth.

The three southern profiles (SWS11, SWS16 and SWS17; ~12.5–24 km) had A and Bw horizon development and sandy loam texture with dark-gray topsoil for SWS11 and brown for SWS16 and SWS17 (Table1 and Fig. 5). Subsoils of the three profiles had redder hues (e.g., 2.5YR–5YR) with stronger chromas (e.g., 3–6), gravelly sandy loam textures, and weak fine granular structure. Field observation showed that SWS16 and SWS17 profiles were derived from vesicular trachyandesite (Fig. 3a, c, d) and breccia (Fig. 3b) that retained their lapilli to bomb-size structures. Profile SWS11 was derived from basaltic-andesite composition (Fig. 2c) intermixed breccia/tephra/lava. The base of the three profiles consisted of loose tephra from the 1815 eruption and the underlying paleosol was not reached within the examined profiles (Fig. 5).

3.2. Soil physical and chemical properties

The overall mean bulk density ($\pm$std dev) of solum horizons across all soils was 1.1 ± 0.2 g cm^{-3} with a range of 0.8–1.4 g cm^{-3} (Table 2). This solum bulk density was similar to the mean bulk density of 1.0 ± 0.1 g cm^{-3} for the several C horizons comprising the SWS15 profile. Mean solum clay content ranged from 4 to 21%, which compares to mean C horizon (parent material) values of 6% and 10% for SWS2 and SWS15. In contrast, the clay content of the paleosol horizons in SWS2 was 31–35%, which was much higher than the overlying modern soil. Soluble cation/anion concentrations were very low as assessed by electrical conductivity values < 0.151 dS m^{-1} across all profiles.

Water pH values (pH$_{H2O}$) for all solum (i.e., A and B) horizons were neutral to slightly alkaline within the range of 7.1–7.6 (Table 2).

Notably, the C horizons of SWS2 were slightly acidic (6.4–6.6), whereas the C horizons of SWS15 were moderately to strongly alkaline (7.6–9.0). The pH$_{KCl}$ values were generally 1 to 1.5 units lower than pH$_{H2O}$, but no pH$_{KCl}$ values were < 5.0 where exchangeable Al^{3+} levels might become a toxicity concern.

Organic carbon concentrations of A horizons ranged from 3.1 to 31.6 g kg^{-1}, whereas Bw horizons ranged from 1.6 to 17.8 g kg^{-1}. Total N concentrations of A horizons ranged from 0.3 to 1.6 g kg^{-1} and Bw horizons ranged from 0.2 to 1.1 g kg^{-1}. Organic C and total N stocks in modern soil horizons to a depth of 100 cm (or depth to paleosol) ranged from 2.3 to 12.8 kg C m^{-2} and 0.21–0.77 kg N m^{-2} (Fig. 6). These stocks translate to C and N accumulation rates over the 200 years of pedogenesis of 11.4–63.4 g C m^{-2} yr^{-1} and 1.0–3.8 g N m^{-2} yr^{-1}.

Phosphorus retention in modern solum horizons ranged from 17.5 to 43.4% across all profiles (Table 3), with the highest values in A or Ap horizons that varied between 33 and 43%. Notably, P-retention in C horizons of SWS2 was < 2%, whereas C horizons in SWS15 had values of 11–24%. Bicarbonate extractable P (Olsen-P) was highly variable among profiles with solum values ranging from 7 to 11 mg P$_2$O$_5$ kg^{-1} (SWS15) to 18–25 mg P$_2$O$_5$ kg^{-1} (SWS11) and 40 mg P$_2$O$_5$ kg^{-1} (A horizon of SWS2). In contrast, HCl-extractable P$_2$O$_5$ values in the solum were similar among profiles with an overall range of 1720–2860 mg P$_2$O$_5$ kg^{-1}. Notably, HCl-extractable P$_2$O$_5$ values in C horizons (SWS2 and SWS15) were relatively high, ranging from 2170 to 3050 mg P$_2$O$_5$ kg^{-1}.

Exchangeable cation concentrations of the modern solum followed (cmol$_c$ kg^{-1}) Ca^{2+} (0.55–6.82) > Mg^{2+} (0.24–2.24) > K$^+$ (0.12–1.11) > Na$^+$ (0.09–0.20). Base saturation percentages of the modern solum were similar among profiles and fell within a range of 30–56%. HCl-extractable K$_2$O values in the solum were high, ranging

Table 2

Selected physiochemical properties of soils formed from the 1815 eruption of Mt. Tambora.

| Profile/ Horizon	Depth	Particle size			BD	pH 1:5		OM		EC
		Sand	Silt	Clay		H$_2$O	KCl	C	N	
	cm	%			g cm^{-3}			g kg^{-1}		dS m^{-1}
SWS2 Typic Ustivitrand (93 m asl)										
Ap	0–22/27	32	47	21	1.19	7.2	5.5	10.0	0.6	0.046
C1	22/27–43/45	88	6	6	1.16	6.6	5.3	2.4	0.2	0.022
C2	43/45–45/50	36	58	6	1.01	6.5	5.2	1.2	0.1	0.028
C3	45/50–52/54	92	1	7	nd	6.4	5.2	1.2	0.1	0.024
C4	52/54–57	66	28	6	0.92	6.5	5.3	1.3	0.1	0.027
2Ab1	57–83	18	51	31	nd	6.4	5.1	6.0	0.5	0.034
2Bb2	83–125	17	48	35	nd	6.6	5.2	5.5	0.5	0.038
SWS16 Dystric Vitric Haplustand (157 m asl)										
A	0–15	57	36	7	1.1	7.3	6.0	19.7	1.3	0.063
Bw1	15–39/53	64	30	6	1.2	7.2	5.9	8.3	0.7	0.022
Bw2	39/53–78	63	31	6	1.2	7.2	5.9	4.2	0.4	0.016
Bw3/C1	78–97	64	28	8	1.1	7.2	5.8	5.2	0.5	0.021
Bw4/C2	97–130	62	33	5	1.1	7.2	5.8	5.6	0.6	0.019
SWS17 Dystric Vitric Haplustand (32 m asl)										
A	0–20	60	35	5	1.2	7.3	5.9	31.6	1.6	0.085
Bw1	20–55	61	32	7	1.3	7.4	6.0	17.8	1.1	0.060
Bw2/C1	55–85	58	38	5	1.2	7.5	6.2	4.7	0.4	0.022
Bw3/C2	85–100	58	38	3	1.0	7.6	6.4	4.8	0.4	0.020
Bw4/C3	100–130	58	40	2	0.9	7.6	6.5	5.3	0.5	0.030
SW11 Dystric Vitric Haplustand (27 m asl)										
A	0–30	47	35	18	1.0	7.1	5.7	3.1	0.3	0.109
Bw1	30–62	62	22	15	1.4	7.2	5.9	2.2	0.2	0.027
Bw2/C1	62–97	64	30	7	1.3	7.4	6.1	1.6	0.2	0.025
Bw3/C2	97–110	54	37	10	1.3	7.3	6.1	2.9	0.3	0.024
SWS15 Dystric Vitric Haplustand (48 m asl)										
A	0–20	39	52	9	1.1	7.4	5.9	11.5	0.9	0.039
Bw	20–37/42	27	64	9	0.8	7.6	6.0	4.4	0.4	0.021
C1	37/42–55	46	45	9	1.0	7.6	6.1	3.9	0.3	0.022
C2	55–72	50	38	12	1.1	8.2	7.0	8.1	0.7	0.092
C3	72–81	34	62	4	0.9	8.3	7.3	7.8	0.7	0.095
C4	81–89	60	29	11	1.1	8.4	7.6	6.5	0.6	0.117
C5	89–99	51	38	10	1.0	8.7	7.9	4.7	0.4	0.102
C6	99–133	71	16	13	1.1	9.0	8.1	4.0	0.4	0.151

Note: nd = not determined.
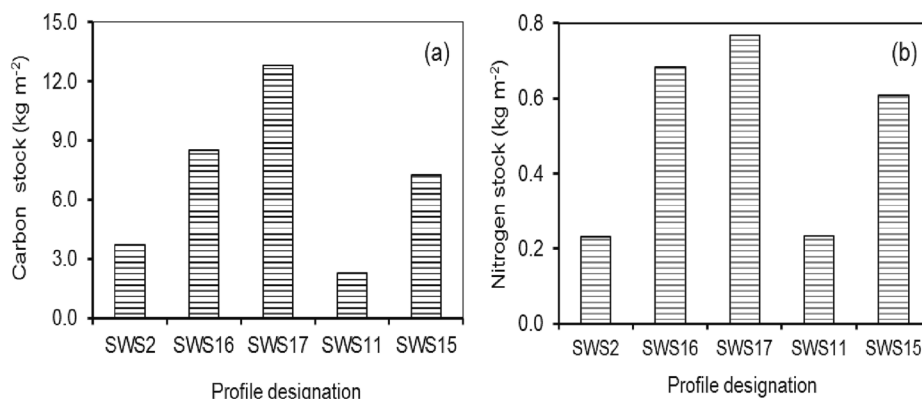
Fig. 6. Accumulation of soil organic carbon and total nitrogen in upper one meter of representative profiles after 200 years of Tambora eruption: (a) total carbon stock, and (b) total N stock. The exception is SWS2 profile where the C and N stocks were from a profile depth of 57 cm corresponding to the modern soil thickness.

Table 3
Selected chemical properties of soils formed from the 1815 eruption of Mt. Tambora.

Profile/ Horizon	Depth	HCl 25% P$_2$O$_5$	K$_2$O	Olsen P$_2$O$_5$	P Ret.	Ca^{2+}	Mg^{2+}	K$^+$	Na$^+$	Sum cation	CEC	BS x
	cm	mg kg^{-1}		mg kg^{-1}	%	cmol$_c$ kg^{-1}						%
SWS2 Typic Ustivitrand (93 m asl)												
Ap	0–22/27	2670	1790	40	33.7	6.82	2.24	1.11	0.20	10.37	21.0	49
C1	22/27–43/45	2740	1310	31	1.2	2.91	0.63	0.23	0.13	3.90	4.37	89
C2	43/45–45/50	3050	2060	41	1.3	2.94	0.61	0.40	0.23	4.18	4.82	87
C3	45/50–52/54	2520	1020	28	1.6	3.31	0.69	0.23	0.28	4.51	5.47	82
C4	52/55–57	2420	1630	25	1.1	2.84	0.58	0.34	0.22	3.98	4.43	90
2Ab1	57–83	2020	1630	22	24.2	15.42	4.46	0.36	0.33	20.57	24.3	85
2Bb2	83–125	1490	1650	17	20.6	19.35	5.55	0.38	0.29	25.57	27.8	92
SWS16 Dystric Vitric Haplustand (157 m asl)												
A	0–15	1970	580	7	40.1	1.60	0.66	0.23	0.18	2.67	7.19	37
Bw1	15–39/53	2290	830	4	26.5	0.68	0.32	0.16	0.16	1.32	4.08	32
Bw2	39/53–78	2540	1330	5	17.7	0.55	0.24	0.12	0.14	1.05	3.18	33
Bw3/C1	78–97	2700	3110	4	20.4	0.71	0.31	0.30	0.16	1.48	4.43	33
Bw4/C2	97–130	2860	1870	3	20.8	0.99	0.44	0.19	0.15	1.77	5.82	30
SWS17 Dystric Vitric Haplustand (32 m asl)												
A	0–20	2290	1640	20	34.6	3.58	1.66	0.65	0.15	6.04	14.4	42
Bw1	20–55	2280	1580	9	28.9	2.56	1.29	0.50	0.19	4.84	11.6	42
Bw2/C1	55–85	2610	1000	6	18.4	1.11	0.49	0.19	0.15	1.94	4.28	45
Bw3/C2	85–100	2520	930	7	17.5	0.84	0.40	0.16	0.13	1.53	3.14	49
Bw4/C3	100–130	2370	830	7	18.4	0.71	0.33	0.14	0.14	1.32	2.65	50
SW11 Dystric Vitric Haplustand (27 m asl)												
A	0–30	2130	1100	18	43.4	1.85	0.84	0.21	0.16	3.06	6.37	48
Bw1	30–62	2290	1190	20	26.7	1.72	0.83	0.14	0.12	2.81	5.59	50
Bw2/C1	62–97	2400	1220	23	23.6	1.36	0.60	0.15	0.11	2.22	4.00	56
Bw3/C2	97–110	2550	1270	25	19.5	1.61	0.81	0.18	0.11	2.71	4.93	55
SWS15 Dystric Vitric Haplustand (48 m asl)												
A	0–20	2020	1620	7	32.9	2.65	0.76	0.35	0.10	3.86	8.94	43
Bw	20–37/42	1720	1140	11	25.6	1.81	0.52	0.34	0.09	2.76	6.23	44
C1	37/42–55	2180	1680	6	20.3	1.65	0.47	0.40	0.17	2.69	5.76	47
C2	55–72	2550	1590	6	21.2	7.35	0.45	0.34	0.11	8.25	6.19	47
C3	72–81	2170	1320	12	23.4	10.85	0.46	0.45	0.16	11.92	6.03	180
C4	81–89	2630	1700	8	21.7	9.29	0.52	0.43	0.15	10.39	5.76	133
C5	89–99	2680	1750	7	24.3	10.61	0.61	0.51	0.18	11.91	5.21	198
C6	99–133	2800	1630	8	11.3	7.41	0.64	0.74	0.31	9.10	4.82	229

BS = base saturation.

from 580 to 3110 mg K$_2$O kg^{-1}, with most values similar to the concentrations in non-weathered C horizons (1020–2060 mg K$_2$O kg^{-1}; SWS2 and SWS15). In the paleosol, exchangeable Ca^{2+} (15.4–19.4 cmol$_c$ kg^{-1}) and Mg^{2+} (4.5–5.6 cmol$_c$ kg^{-1}) values were much higher.

3.3. Soil mineralogy of sand fraction and amorphous materials

The mineralogical composition of the 50–250 μm sand fraction, fresh and weathered trachyandesite, and fresh basaltic-andesite lava are shown in Table 4. The fresh vesicular trachyandesite and basaltic-

andesite lava had very similar mineralogical compositions: opaque minerals > volcanic glass > glassy aggregates > labradorite > augite. In contrast, the weathered trachyandesite displayed a distinct decrease in volcanic glass and glassy aggregates with a corresponding increase in non-distinguishable weathered minerals, augite and labradorite. Four of the soil profiles (SWS 2, 15, 16, and 17) had similar mineral composition in the sand fraction with a dominance of opaque minerals, labradorite, augite and volcanic glass/glassy aggregates. Profile SWS11 was distinctly different having a higher volcanic glass/glassy aggregate content and correspondingly lower opaque and labradorite minerals

Table 4

Mineralogical composition of the 50–250 µm sand fraction of soils, fresh and weathered trachyandesite, and fresh basaltic andesite lava from the 1815 eruption of Mt. Tambora.

Sample/ horizon	Depth cm	Op %	Qz	Wm	Rf	Vg	Lb	Bn	Sn	Bt	Hb	Au	Hp	Tu	Sum
SWS2 Typic Ustivitrand (93 m asl)															
Ap	0–22/27	34	< 1	< 1	14	3	21	2	< 1	dt	6	18	2	nd	100
C1	22/27–43/45	21	nd	< 1	19	9	29	< 1	dt	3	2	16	1	nd	100
C2	43/45–45/50	15	nd	nd	28	11	32	nd	< 1	1	1	12	< 1	nd	100
C3	45/50–52/58	9	nd	< 1	39	8	34	< 1	nd	< 1	1	9	–	nd	100
C4	52/55–57	16	nd	nd	41	5	25	nd	nd	nd	< 1	13	< 1	nd	100
2Ab1	57–83	41	< 1	< 1	13	3	18	2	< 1	nd	8	15	1	nd	101
2Bb2	83–125	47	dt	dt	5	2	13	1	< 1	nd	15	17	< 1	nd	100
SWS16 Dystric Vitric Haplustand (157 m asl)															
A	0–15	24	nd	8	19	1	23	1	nd	1	1	22	< 1	nd	100
Bw1	15–39/53	27	nd	12	17	< 1	20	2	nd	1	< 1	21	nd	nd	100
Bw2	39/53–78	31	nd	10	15	1	17	1	nd	2	nd	23	nd	nd	100
Bw3/C1	78–97	24	nd	16	25	< 1	15	< 1	nd	1	nd	19	< 1	nd	100
Bw4/C2	97–130	32	nd	18	18	nd	16	< 1	nd	2	nd	14	nd	nd	100
SWS17 Dystric Vitric Haplustand (32 m asl)															
A	0–20	35	< 1	4	19	5	15	1	nd	< 1	nd	21	< 1	< 1	100
Bw1	20–55	39	nd	3	11	5	17	1	< 1	1	nd	23	nd	nd	100
Bw2/C1	55–85	34	< 1	8	19	3	18	3	< 1	1	nd	14	nd	nd	100
Bw3/C2	85–100	31	nd	11	28	2	14	2	nd	< 1	nd	12	nd	nd	100
Bw4/C3	100–130	32	nd	7	21	2	16	3	< 1	2	nd	17	< 1	nd	100
SWS11 Dystric Vitric Haplustand (27 m asl)															
A	0–30	5	nd	6	38	27	5	3	nd	1	1	13	< 1	1	100
Bw1	30–62	5	nd	9	37	25	6	2	nd	< 1	< 1	15	nd	1	100
Bw2/C1	62–97	3	nd	14	44	22	4	2	nd	< 1	< 1	11	nd	< 1	100
Bw3/C2	97–110	2	nd	15	49	20	3	1	nd	< 1	< 1	10	nd	< 1	100
SWS15 Dystric Vitric Haplustand (48 m asl)															
A	0–20	19	nd	< 1	25	13	21	1	nd	1	2	18	< 1	nd	100
Bw	20–37/42	25	< 1	1	16	15	18	< 1	< 1	< 1	1	24	nd	nd	100
C1	37/42–55	22	< 1	2	19	14	23	1	< 1	2	< 1	17	nd	nd	100
C2	55–72	17	nd	1	29	9	26	1	< 1	nd	1	16	< 1	nd	100
C3	72–81	28	nd	1	16	6	21	1	nd	2	< 1	25	nd	nd	100
C4	81–89	27	nd	< 1	18	7	24	< 1	nd	1	< 1	23	< 1	nd	100
C5	89–99	24	nd	2	23	8	25	1	nd	< 1	nd	17	< 1	nd	100
C6	99–133	21	< 1	1	26	11	19	< 1	< 1	< 1	nd	22	nd	nd	100
Fresh trachyandesite (Rft), weathered vesicular trachyandesite (Rw) and basaltic andesite lava (Abf)															
Rft	0	33	< 1	1	19	22	12	1	nd	1	nd	11	nd	nd	100
Rw	40–60	28	nd	17	11	4	18	2	nd	5	nd	15	nd	nd	100
Abf	0	34	nd	1	15	26	13	1	nd	1	< 1	9	nd	nd	100

Op = opaque mineral; Qz = Quartz; Wm = weathered minerals; Rf = rock fragment (glassy aggregates); Vg = Volcanic glass; Bn = bytownite; Sn = sanidine; Lb = Labradorite; Bt = Biotite; Hb = hornblende; Au = augite; Hp = hypersthene; Tu = tourmaline; nd = not detected.

contents. Quartz represented < 1% of the sand fraction of all soil samples, consistent with the fresh vesicular trachyandesite and basaltic-andesite lava as parent materials (Table 4). For the paleosol underlying the SWS2 modern profile, the primary mineral composition showed distinct changes in the proportion of minerals, but contained the same mineral assemblage as the overlying modern soil. The trend in mineral proportions showed a marked increase in opaque mineral and hornblende from modern soil to paleosol, whereas glassy minerals, volcanic glass and labradorite decreased.

Given the low degree of chemical weathering in these young deposits, the extraction values for short-ranged order (SRO) and amorphous materials were very low (<1–23 g kg^{-1}) (Table 5). Coupled with the lack of complete specificity among the selective dissolution extractants, a strict interpretation of results becomes somewhat tenuous for some constituents (Rennert, 2019). Pyrophosphate-extractable Fe, Al and C provide an estimate of metal-humus complexes. Concentrations of Al_p and Fe_p in A horizons were within the range of 0.67–3.51 g Al kg^{-1} and 0.08–1.04 g Fe kg^{-1}, whereas B horizons values ranged between 0.02 and 0.80 g Al kg^{-1} and 0.01–0.07 g Fe kg^{-1} (Table 5). Concentrations of C_p in A and B horizons were (mean ± std dev; range) 3.9 ± 1.9 (1.0 – 6.2) g kg^{-1} and 2.9 ± 1.3 (1.0–5.2) g kg^{-1}, respectively. The C_p contribution to total C represented $30 \pm 10\%$ in A horizons and $55 \pm 18\%$ in B horizons indicating generally more humified organic matter that is associated with the metals in B horizons. In assessing the $(Fe_p + Al_p)/C_p$ atomic ratio, A horizon values demonstrated large variability (0.06–0.73), whereas B horizons had more uniform values across profiles (0.01–0.14). In the paleosol of SWS2, pyrophosphate extractable Fe, Al and C increased sharply from the overlying modern soil.

Oxalate-extractable Fe, Al and Si derive primarily from metal-humus complexes, allophanic materials (e.g., allophane, imogolite) and SRO Fe (hydr)oxides (e.g., ferrihydrite). The Fe_o concentrations of A horizons (mean ± std dev; 6.27 ± 4.44 g kg^{-1}) were greater than B horizons (2.69 ± 1.90 g kg^{-1}), but both were lower than C horizons (9.85 ± 4.62 g kg^{-1}). Similarly, Al_o concentrations of A horizons (6.06 ± 2.06 g kg^{-1}) were greater than B horizons (2.89 ± 1.30 g kg^{-1}); however, in contrast to Fe_o, C horizon Al_o values (2.08 ± 0.67 g kg^{-1}) were lower than A/B horizon concentrations. The Si_o concentrations (g kg^{-1}) were consistently low across A (0.93 ± 0.30, B (0.25 ± 0.16) and C (0.46 ± 0.37) horizons indicating no appreciable formation of allophanic materials.

Dithionite-extractable Fe and Mn derive from crystalline and SRO metal (hydro)oxides, as well as metal-humus complexes. The Fe_d concentrations of A horizons (4.47 ± 0.79 g kg^{-1}) were greater than B horizons (0.82 ± 0.83 g kg^{-1}), with intermediate concentrations in C horizon (2.59 ± 0.75 g kg^{-1}) (Table 5). Notably, Fe_o concentrations were unexpectedly higher than Fe_d concentrations, which we attribute to the ability of oxalate to extract Fe from several opaque minerals (e.g., magnetite, maghemite) that were prevalent in the parent materials (Dahlgren, 1994). The Mn_d concentrations (g kg^{-1}) displayed a similar

Table 5
Selective dissolution and estimated ferrihydrite and allophane contents of soils from the 1815 eruption of Mt. Tambora.

Profile/ Horizon	Depth	Dithionite		Oxalate			Pyrophosphate			$Fe_p + Al_p)/C_p$	Ferri-hydrite	Allo-phane
		Fe_d	Mn_d	Fe_o	Al_o	Si_o	Fe_p	Al_p	C_p			
	cm	g kg^{-1}		g kg^{-1}			g kg^{-1}				%	%
SWS2 Typic Ustivitrand (93 m asl)												
Ap	0–22/27	9.33	0.91	14.13	4.50	0.75	1.04	3.51	4.3	0.52	2.40	0.5
C1	22/27–43/45	2.56	0.46	8.80	2.11	0.41	0.11	1.19	0.1	na	1.50	0.3
C2	43/45–45/50	2.93	0.34	14.30	2.37	0.87	0.19	1.60	0.2	na	2.43	0.5
C3	45/50–52/54	1.96	0.09	12.22	2.06	0.40	0.17	1.09	0.1	na	2.08	0.4
C4	52/54–57	3.86	0.51	20.60	2.20	1.35	0.15	1.69	1.0	na	3.50	0.7
2Ab1	57–83	15.40	1.93	18.35	8.12	0.83	2.67	4.03	4.6	0.60	3.12	1.3
2Bb2	83–125	19.60	2.50	13.33	21.15	0.82	8.84	3.09	5.2	0.55	2.27	1.3
SWS16 Dystric Vitric Haplustand (157 m asl)												
A	0–15	3.35	0.07	3.44	6.98	0.92	0.12	1.36	4.1	0.15	0.58	1.5
Bw1	15–39/53	0.72	0.04	1.89	3.07	0.22	0.02	0.41	3.1	0.06	0.32	0.3
Bw2	39/53–78	0.12	0.01	0.87	2.80	0.17	0.01	0.15	3.1	0.02	0.15	0.3
Bw3/C1	78–97	0.43	0.03	0.45	3.31	0.32	0.01	0.16	3.1	0.02	0.08	0.5
Bw4/C2	97–130	0.63	0.01	0.36	3.21	0.29	0.01	0.17	4.2	0.02	0.06	0.5
SWS17 Dystric Vitric Haplustand (32 m asl)												
A	0–20	4.01	0.10	4.52	6.74	0.73	0.10	0.86	6.2	0.06	0.77	1.2
Bw1	20–55	1.93	0.05	4.33	6.06	0.64	0.07	0.80	5.2	0.07	0.74	1.0
Bw2/C1	55–85	0.49	0.06	1.78	3.16	0.08	0.02	0.06	3.1	0.01	0.30	0.1
Bw3/C2	85–100	2.43	0.07	2.07	3.20	0.06	0.01	0.03	3.1	0.01	0.35	0.1
Bw4/C3	100–130	0.99	0.03	1.13	3.38	0.10	0.01	0.02	4.2	0.00	0.19	0.2
SWS11 Dystric Vitric Haplustand (27 m asl)												
A	0–30	2.75	0.10	4.03	8.61	1.45	0.11	1.59	1.0	0.73	0.68	2.3
Bw1	30–62	0.52	0.02	4.72	1.54	0.34	0.02	0.33	2.1	0.14	0.80	0.5
Bw2/C1	62–97	0.98	0.03	4.90	1.26	0.24	0.01	0.18	1.0	0.08	0.83	0.4
Bw3/C2	97–110	0.13	0.02	5.21	1.05	0.16	0.02	0.08	1.0	0.04	0.89	0.3
SWS15 Dystric Vitric Haplustand (48 m asl)												
A	0–20	2.92	0.08	5.25	4.44	0.78	0.08	0.67	4.1	0.08	0.89	1.3
Bw	20–37/42	1.99	0.06	4.61	2.65	0.34	0.05	0.38	3.1	0.06	0.78	0.5
C1	37/42–55	1.74	0.06	5.96	2.11	0.14	0.04	0.14	2.1	na	1.01	0.2
C2	55–72	3.36	0.07	6.78	2.14	0.25	0.02	0.04	3.1	na	1.15	0.4
C3	72–81	2.18	0.07	6.26	2.82	0.34	0.04	0.08	3.3	na	1.06	0.4
C4	81–89	2.92	0.07	7.58	2.43	0.25	0.04	0.05	3.1	na	1.29	0.5
C5	89–99	1.47	0.06	7.40	2.82	0.28	0.03	0.04	3.2	na	1.26	0.4
C6	99–133	2.93	0.06	8.59	2.87	0.32	0.04	0.03	2.1	na	1.46	0.5

Note: Ferrihydrite % = 1.7 × Fe_{ox}% (Parfitt and Childs, 1988); Allophane % = A × Si_{ox} (Parfitt, 1990), (A is the factor for estimation varied from 5 to 16 depending on $(Al_o − Al_p):Si_o$ ratio with A equals to 5 at 1:1 ratio and is 16 for 3.5:1. ratio or higher. na = not applied.

overall profile distribution to Fe_d in A (0.25 ± 0.37), B (0.04 ± 0.02) and C (0.18 ± 0.18) horizons. Given the redox sensitive nature of Fe and Mn, the elevated Fe_d and Mn_d concentrations in the SW2 C4 horizon overlaying the clay-rich paleosol horizons likely reflect impeded water drainage (i.e., periodic anoxic conditions) at the interface between the modern soil and paleosol. In the SWS2 paleosol horizons, dithionite-extractable Fe, Al and Mn increased sharply, indicating more advanced soil development.

3.4. Chemical weathering indices

Based on SiO_2 content, the trachyandesite has a typical andesite content of 57.5% (andesite range: 52–66%), whereas the basaltic-andesite lava has a SiO_2 content (53.3%) near the andesite-basalt boundary (basalt range: 45–52%) (Table 6). Further comparison of the two parent materials shows the trachyandesite to have higher Na, K and P contents and lower Fe and Ca than the basaltic-andesite lava. Given the variability in vertical distribution of elemental concentrations among individual horizons within each profile, no distinct patterns emerged for elemental changes due to chemical weathering either within or between profiles (Table 6). This suggests that the erupted materials of Tambora are relatively uniform in chemical composition.

A number of chemical weathering indices were employed to assess the relative degree of chemical weathering compared to the unweathered tephra/lava parent materials. These weathering indices assume a depletion of silicon or base cations (Ca^{2+}, Mg^{2+}, K^+, Na^+) relative to aluminum and/or iron, which are assumed to accumulate *in situ* at the near neutral pH values prevalent in the examined soils. In spite of the

differences in chemistry between the trachyandesite and basaltic-andesite lava parent materials, their reference index values were similar (Table 7).

Chemical index of alteration (CIA) values increased as chemical weathering progressed, consistent with the trend of A horizons (48.4 ± 4.6) > B horizons (45.4 ± 2.4) > C horizons (43.8 ± 4.2) ≈ tephra/lava (43.1) (Table 7). Base depletion index (BDI) values decreased as base cations are released by weathering and displayed the expected trend of A horizons (1.13 ± 0.18) < B horizons (1.25 ± 0.09) < C horizons (1.34 ± 0.20) ≈ tephra/lava (1.35). Further, the two desilication indices (DSI-R1 and DSI-R2) showed a decreasing trend with A horizons (4.81 ± 0.63/3.80 ± 0.45) < B horizons (4.97 ± 0.54/3.93 ± 0.36) < C horizons (5.14 ± 0.55/4.05 ± 0.29) ≈ tephra/lava (5.24/4.16). A comparison of the SWS2 modern soil versus its underlying paleosol demonstrated higher values for CIA and lower values for BDI, DSI-R1 and DSI-R2 in the paleosol, corresponding to its more advanced chemical weathering state (Table 7). All of these weathering indices clearly distinguished the strongly contrasting degree of chemical weathering between the modern soil and its underlying paleosol.

4. Discussion

4.1. Soil morphological features

Soil morphological features showed that the soils developed from highly explosive pyroclastic materials that varied from shallow deposits on the western flank to deeper deposits on the eastern and southern flanks (Figs. 4 and 5). Stratification of pyroclastic materials in SWS2 and

Table 6
Total macro-elemental composition of soils and their parent materials from the 1815 eruption of Mt. Tambora.

Profile/	Depth	SiO$_2$	Al$_2$O$_3$	Fe$_2$O$_3$	Na$_2$O	CaO	K$_2$O	MgO	TiO$_2$	P$_2$O$_5$	MnO	SO$_3$
Horizon	Cm	%										
SWS2 Typic Ustivitrand (93 m asl)												
Ap	0–22/27	52.07	22.46	10.08	3.34	4.80	3.27	2.12	0.92	0.42	0.22	0.07
C1	22/27–43/45	53.89	21.15	7.60	4.27	5.08	4.38	2.03	0.72	0.42	0.19	0.09
C2	43/45–45/50	55.87	20.35	6.25	4.98	4.45	4.99	1.62	0.62	0.41	0.18	0.08
C3	45/50–52/54	53.86	20.57	6.68	4.84	5.62	4.88	1.88	0.65	0.40	0.18	0.11
C4	52/54–57	55.62	20.47	6.16	5.12	4.43	5.04	1.68	0.63	0.40	0.19	0.07
2Ab1	57–83	53.12	23.75	11.92	2.21	2.83	2.72	1.33	1.18	0.35	0.30	0.11
2Bb2	83–125	52.02	23.81	13.94	1.85	2.22	2.59	1.33	1.34	0.29	0.34	0.11
SWS16 Dystric Vitric Haplustand (157 m asl)												
A	0–15	55.04	20.20	6.83	4.13	5.65	4.53	2.11	0.67	0.45	0.17	0.09
Bw1	15–39/53	54.32	20.19	6.75	4.55	5.83	4.57	2.19	0.64	0.43	0.17	0.16
Bw2	39/53–78	50.29	20.10	9.32	5.61	5.72	4.73	2.36	0.88	0.39	0.25	0.06
Bw3/C1	78–97	52.82	20.20	8.16	5.18	5.36	4.39	2.18	0.80	0.40	0.21	0.06
Bw4/C2	97–130	53.58	20.19	7.70	4.89	5.51	4.39	2.12	0.76	0.39	0.20	0.05
SWS17 Dystric Vitric Haplustand (32 m asl)												
A	0–20	55.42	17.56	8.45	3.15	5.94	4.93	2.13	0.52	0.58	0.17	0.28
Bw1	20–55	55.71	17.30	7.81	3.80	5.95	4.99	2.21	0.48	0.51	0.20	0.05
Bw2/C1	55–85	55.70	17.29	7.64	3.94	6.03	4.90	2.28	0.47	0.51	0.19	0.04
Bw3/C2	85–100	55.78	17.25	7.58	3.96	6.02	4.93	2.25	0.47	0.49	0.19	0.04
Bw4/C3	100–130	55.76	17.32	7.54	3.99	6.04	4.84	2.27	0.47	0.51	0.18	0.04
SW11 Dystric Vitric Haplustand (27 m asl)												
A	0–30	55.17	20.36	6.90	4.33	5.10	4.52	2.01	0.68	0.44	0.19	0.08
Bw1	30–62	54.45	20.15	7.18	4.34	5.57	4.58	2.18	0.70	0.41	0.18	0.08
Bw2/C1	62–97	53.98	20.10	7.09	4.43	5.88	4.70	2.20	0.70	0.41	0.18	0.09
Bw3/C2	97–110	56.91	19.25	7.27	2.47	5.67	4.33	2.48	0.70	0.40	0.18	0.11
SWS15 Dystric Vitric Haplustand (48 m asl)												
A	0–20	56.03	17.35	8.10	3.57	5.72	5.20	2.25	0.50	0.56	0.20	0.07
Bw	20–37/42	55.58	16.27	8.69	3.54	5.42	6.17	2.01	0.52	0.43	0.25	0.06
C1	37/42–55	56.00	17.28	7.77	3.91	5.89	5.05	2.42	0.47	0.49	0.19	0.04
C2	55–72	54.23	16.56	8.26	3.64	7.13	5.23	2.70	0.54	0.51	0.20	0.05
C3	72–81	54.87	17.13	7.82	3.81	7.08	4.85	2.43	0.49	0.51	0.19	0.05
C4	81–89	55.21	15.96	8.44	3.71	6.90	6.16	2.05	0.52	0.41	0.24	0.06
C5	89–99	54.79	17.05	7.72	3.83	7.33	4.85	2.48	0.49	0.49	0.19	0.04
C6	99–133	54.35	17.06	8.00	3.74	7.67	4.70	2.63	0.51	0.52	0.19	0.04
Fresh vesicular trachyandesite (Rft) and **basaltic andesite lava** (Abf)												
Rft	0	57.50	17.20	6.85	4.08	4.89	5.60	1.88	0.43	0.51	0.20	0.05
Abf	0	53.26	18.91	7.87	3.40	8.71	4.28	1.90	0.41	0.43	0.15	0.02

Notes: Data are reported on a "Loss On Ignition"-free basis; Rft = Fresh vesicular trachyandesite on soil surface; Abf = Fresh basaltic andesite lava; Criteria: Basalt 49–53% SiO$_2$; basaltic andesite: 53–57% SiO$_2$

SWS15 was attributed to the sequence of eruptions phases that produced interlayering of tephra, pumice and pyroclastic flow deposits (Abrams and Sigurdsson, 2007). In contrast, the volcanic deposits on the southern flank (SWS11, SWS16, SWS17) had a relatively uniform sandy loam texture throughout the entire soil profile (Fig. 5) accompanied by reddish color that indicates more soil development (Torrent et al., 1983).

Solum depth plays a critical role in agricultural productivity as the solum serves as the primary rooting zone providing nutrients and water to plants. Solum depth/development was lowest on the western flank (SWS2: 25 cm), intermediate on the eastern flank (SWS15: 40 cm) and greatest on the southern flank (SWS11, SWS16, SWS17: 89–107 cm). Solum thickness shown here is the A + B horizons, after subtracting the C horizon component from B/C horizons (see example Fig. S4 for separation of C component from B horizons). In particular, the thicker solum development on the southern flank (SWS11, SWS16, SWS17) occurred in thicker eruption deposits having a relatively uniform textural stratigraphy (sandy loam) and reddish color throughout the solum. In contrast, the sharply contrasting particle-size stratification (loams over pumice or coarse sand) within the SWS2 and SWS15 profiles appears to limit solum depth/development. These strongly contrasting particle-size boundaries may limit vertical water flow as capillary action retains the water in the finer-textured materials overlying the coarse deposits. In both the SWS2 and SWS15 profiles, the solum boundary was restricted to the materials above the first occurrence of a strongly contrasting particle-size transition. Hence, we posit that the sharp difference in textural stratigraphy of the parent material is the strongest factor controlling solum depth.

Rates of solum formation provide an important metric when considering soil rejuvenation for agricultural purposes following major soil perturbations. Based on the solum depths and 200 years of post-eruption development, we calculated solum developmental rates of 1.2 to 5.3 mm yr^{-1} as a metric of soil formation. These rates were very high relative to several previous analyses, which generally fall in the 0.0001 and 0.6 mm yr^{-1} range (Stockmann et al., 2014). Importantly, the methods for assessing soil formation rates are operationally-defined and therefore are not directly comparable. For example, Stockmann et al. (2014) used terrestrial cosmogenic nuclides (^{10}Be) to determine soil formation rates of 0.0001 and 0.6 mm yr^{-1} (n = 226), whereas Wakatsuki and Rasyidin (1992) used a geochemical mass balance to determine rates of soil formation of 0.03 to 0.103 mm yr^{-1}. However, soil formation would be expected to be appreciable greater in highly weatherable, unconsolidated materials, such as pyroclastic materials. In fact, solum developmental rates in pumiceous tuff from the 1883 Krakatau eruption were 1.2 to 2.5 mm yr^{-1} after 100 years of soil genesis (Hardjowigeno, 1992). Further, a chronosequence assessment of soil developmental rates by Bockheim (1980) found that solum depth was greater at higher temperatures (isohyperthermic conditions in this study) and increased following a logarithmic function over time suggesting that the initially high solum developmental rates will rapidly decrease with increasing time. Overall, the high solum developmental rates in the Tambora pyroclastic materials led to a rapid recovery of soil functions to support agricultural production.

Table 7
Weathering indices of soil profiles formed from the 1815 eruption of Mt. Tambora.

Profile/ Horizon	Depth cm	Weathering indices			
		CIA[†]	BDI[‡]	DSI-R1[§]	DSI-R2[¶]
SWS2 Typic Ustivitrand					
Ap	0–22/27	55.8	0.83	3.94	3.06
C1	22/27–43/45	50.1	1.05	4.33	3.52
C2	43/45–45/50	48.4	1.10	4.67	3.90
C3	45/50–52/54	46.7	1.19	4.45	3.69
C4	52/54–57	48.3	1.11	4.62	3.88
2Ab1	57–83	66.9	0.49	3.80	2.88
2Bb2	83–125	70.6	0.41	3.71	2.70
SWS16 Dystric Vitric Haplustand					
A	0–15	47.9	1.17	4.63	3.81
Bw1	15–39/53	46.7	1.22	4.57	3.77
Bw2	39/53–78	44.8	1.22	4.25	3.28
Bw3/C1	78–97	46.7	1.16	4.45	3.54
Bw4/C2	97–130	46.9	1.17	4.51	3.63
SWS17 Dystric Vitric Haplustand					
A	0–20	45.1	1.23	5.37	4.11
Bw1	20–55	43.5	1.33	5.48	4.25
Bw2/C1	55–85	43.1	1.36	5.48	4.27
Bw3/C2	85–100	43.0	1.37	5.50	4.29
Bw4/C3	100–130	43.1	1.36	5.47	4.29
SW11 Dystric Vitric Haplustand					
A	0–30	48.9	1.11	4.61	3.79
Bw1	30–62	47.5	1.17	4.59	3.74
Bw2/C1	62–97	46.5	1.22	4.56	3.73
Bw3/C2	97–110	50.2	1.12	5.03	4.05
SWS15 Dystric Vitric Haplustand					
A	0–20	44.2	1.29	5.49	4.23
Bw	20–37/42	42.1	1.32	5.81	4.33
C1	37/42–55	43.3	1.36	5.51	4.28
C2	55–72	40.2	1.53	5.57	4.22
C3	72–81	41.2	1.47	5.45	4.22
C4	81–89	38.6	1.51	5.88	4.40
C5	89–99	40.6	1.51	5.46	4.24
C6	99–133	40.3	1.53	5.42	4.17
Fresh vesicular trachyandesite (Rf) and basaltic andesite lava Abf)					
Rft	0	44.2	1.29	5.68	4.53
Abf	0	42.0	1.41	4.79	3.78

Notes: na = not applied; R1 = Al_2O_3; R2 = $Fe_2O_3 + Al_2O_3$.
Two desilication indices (DSI): [§]DSI-R1 = SiO_2/Al_2O_3 and [¶]DSI-R2 = $SiO_2/(Fe_2O_3 + Al_2O_3)$.
[†] Chemical index of alteration (CIA) = $Al_2O_3/(Al_2O_3 + CaO + Na_2O + K_2O) \times 100$.
[‡] Base depletion index (BDI) = $(CaO + MgO + Na_2O + K_2O)/(Fe_2O_3 + Al_2O_3 + TiO_2)$.

4.2. Chemical weathering

Chemical weathering is rapid in pyroclastic materials owing to the prevalence of highly weatherable volcanic glass, high surface area (silt- and sand-sized particles along with porous pumice) and high permeability (promoting solid-solution interactions) (Shoji et al., 1993a). Weathering is further promoted by the isohyperthermic soil climate regime and the abundance of soil moisture for 7–8 months each year at our study sites. The glass + glassy aggregate content of the unweathered trachyandesite (41%) and basaltic-andesite lava (41%) were slightly higher than the C horizon (35%) materials identified in the various profiles indicating that glassy materials were a dominant component of the parent materials (Table 4). The higher glassy components of the trachyandesite (57.5% SiO_2) than the basaltic-andesite lava (53.3% SiO_2) are important because weathering rates of the glass fraction

display an exponentially decreasing function with increasing Si content (Wolff-Boenisch et al., 2004). Based on the Si content versus weathering relationship determined by Wolff-Boenisch et al. (2004), albeit at pH 4 and 25 °C, the projected lifetimes for the trachyandesite and basaltic-andesite lava glass fractions were 1360 and 975 years, respectively. Weathered trachyandesite taken from the profile at same location as the fresh material showed a marked decrease in the glassy fraction, from 41 to 15%, after 200 years of weathering (Table 4).

Contents of total Si, Al and Ti expressed in oxides showed relatively constant values from the soil surface to the base of all profiles indicating a general homogeneity of parent material elemental composition (Table 6). The chemical weathering indices showed a consistent pattern for desilication and base cation removal, with A horizons being more highly weathered than B horizons. In contrast, the CIA and BDI values for all C horizons (C1-C6) of the SWS15 profile were slightly lower and higher, respectively, compared to the fresh trachyandesite, indicating little chemical alteration and base cation depletion (Table 7). Enhanced weathering in A versus B horizons is consistent with increased biological activity generating increased proton (H_2CO_3 and organic acids) and chelate fluxes. Chemical weathering rates decrease rapidly as weathering proceeds due to the progressive loss of reactive surface sites (fine particles and high-energy sites) (Dahlgren et al., 1999).

4.3. Soil mineralogical characteristics

More easily weatherable minerals (e.g., labradorite, augite and volcanic glass) dominated the sand fraction, whereas quartz was only sporadically present (<1%) (Table 4). These more easily weatherable minerals play an important role in providing "rock-derived" nutrient reserves for agricultural crops. In particular, biotite and apatite are prevalent sources of slow-release K and P, respectively, as reflected in the high total K and P (XRF analysis, Table 6) and high potential available K and P (HCl-extractant) values in both the solum and parent materials (Table 3). The weathering progression associated with the modern soil to paleosol transition was marked by an increased contents of opaque minerals and hornblende, whereas the abundance of glassy minerals, volcanic glass and labradorite decreased. Hence, periodic deposition of shallow layers of pyroclastic materials serves to rejuvenate chemical weathering and the supply of rock-derived nutrients, while still allowing plants to tap into the underlying soil to obtain nitrogen from the organic-matter rich buried horizons (Dahlgren et al., 1990; Dahlgren et al., 2004).

Formation of allophanic materials and other short-range-order (SRO) minerals is common in soils derived from recent volcanic materials throughout Indonesia (Chartres and Van Reuler, 1985; Van Ranst et al., 2002; Anda et al., 2016; Anda and Dahlgren, 2020a, 2020b; Lyu et al. 2022). The SRO minerals are considered early-stage weathering products in soils formed in pyroclastic materials owing to rapid weathering of volcanic glass and glassy aggregates (Wada 1985, 1986; Shoji et al., 1993a, 1993b). Given the low degree of chemical weathering in the young deposits, oxalate-extractable Si indicated very low allophane/imogolite contents (0.1–2.3%) across all solum horizons and the buried paleosol (Table 5). The important pedogenic factors affecting allophanic material formation are the aqueous H^+, Al^{3+} and silicic acid activities (Lyu et al. 2022). Generally, allophane forms from weathering of tephra at $pH_{(H2O)}$ values between 5 and 7 (Parfitt and Kimble, 1989) where carbonic acid is the dominant proton donor (Dahlgren et al., 2004). In laboratory synthesis, precipitates formed at pH > 7 with Al:Si < 1 have almost all of the Al in a tetrahedral network (Parfitt, 2009). All modern solum horizons had pH values higher than 7, indicating relatively unfavorable conditions for allophane formation.

The formation of Al complexes with organic substances may also prevent the formation of allophanic materials. Excluding the SWS2 profile, metal-humus complexes comprised a relatively narrow range of 13–19% (Al_p/Al_o) and 2–4% (Fe_p/Fe_d) in A horizons. Higher ratios were found in the SWS2 A horizon ($Al_p/Al_o = 78\%$ and $Fe_p/Fe_d = 11\%$),

which we attribute to agricultural practices occurring at this site (Fig. S2a). The degree of metal complexation by humic substances is probably more accurately depicted by examining pyrophosphate extractable Al, Fe, and C (Al_p, Fe_p, C_p) using atomic ratios: Al_p/C_p or $(Al_p + Fe_p)/C_p$. Takahashi and Dahlgren (2016) calculated that metal saturation would occur at a metal/C_p atomic ratio of ~ 0.12. Many of the $(Al_p + Fe_p)/C_p$ atomic ratio for Tambora soils fell below this presumed metal-saturation level. With a few exceptions, our results are similar to those found for A horizons of Andosols in which the Al_p/C_p ratio ranged between 0.05 and 0.2 (Higashi, 1983) and the $(Al_p + Fe_p)/C_p$ ratio ranged between 0.1 and 0.2 (Inoue and Higashi, 1988). Importantly, the apparent under-saturation of humic substances suggests that metals released by weathering will be sequestered by the humic substances and not available for synthesis of SRO minerals.

The metal under-saturation of humic substances may result from several factors. First, the rapid accumulation of SOM during the early stages of pedogenesis may exceed the rates of Al/Fe released by weathering. Once SOM stock become stabilized, ongoing metal release should lead to saturation of the SOM complexation capacity resulting in free Al^{3+} and Fe^{3+} available for formation of SRO minerals. Second, the alkaline pH range results in very low metal solubility decreasing the availability of free Al^{3+} and Fe^{3+} for complexation with humic substances. Finally, the ustic soil moist regime results in a distinct period of soil desiccation that favors formation of crystalline minerals (e.g., halloysite, goethite/hematite; Rasmussen et al. 2007; Lyu et al. 2018; Lyu et al., 2022), further decreasing the availability of Al^{3+} and Fe^{3+} for incorporation into SRO minerals. The seasonal desiccation of soils increase solute activities and enhance crystallization of secondary minerals as crystallization is promoted by warmer temperatures and soil dehydration (Schwertmann, 1985; Talibudeen, 1981; Takahashi et al., 1993). This is consistent with a global assessment of allophane occurrence that found allophanic materials most frequently in soils with a udic soil moisture regime, and less frequently in soils with ustic, xeric and aridic soil moisture regimes (Parfitt and Kimble, 1989).

The Fe_o fraction was consistently higher than the Fe_d fraction across all soils, and considerable Fe_o concentrations were extracted from unweathered C horizons. We attribute the high Fe_o concentrations to the partial dissolution of magnetite/maghemite found in the opaque minerals comprising the sand fraction (Algoe et al., 2012; Rennert, 2019). Hence, the Fe_d values appear to provide a more realistic indicator of the active Fe fraction; however, it does not distinguish between the crystalline and poorly crystalline fractions. This becomes especially relevant for soil classification as one criteria for andic properties is based on the active Al and Fe fraction extracted by oxalate ($Al_o + 1/2 Fe_o$). Thus, for classification purposes, when considerable magnetite and maghemite are present, it may be more appropriate to substitute the Fe_d fraction for Fe_o ($Al_o + 1/2 Fe_d$), although this may still result in an overestimation of the active Fe fraction as it includes the crystalline Fe fraction.

4.4. Soil physical and chemical properties

In regions depending on subsistence agriculture, the recovery time for productive agriculture is a critical social and economic consideration following large volcanic eruptions. In thick pyroclastic deposits, such as those from the 1815 Tambora eruption, the soil-forming clock is set back to time zero and requires primary plant succession to reestablish soil organic matter, nutrient cycling and the associated microbial community. Chemical weathering and accumulation of organic matter facilitate development of microbial communities, nutrient cycling, soil structure, water holding capacity and cation/anion retention through CEC/AEC.

4.4.1. Soil physical properties

The particle size and thickness of pyroclastic deposits generally declined with increasing distance from the source (Anda and Sarwani, 2012). The absence of roots below the pumice and coarse sand layers of SWS2 and SWS15 (Fig. 4) may suggest a root-restricting layer owing to either anaerobic conditions above the strongly contrasting particle-size boundaries (e.g., pumice layers and clay-rich paleosol in SWS2), or bridging between pumice particles that restricts root proliferation (Cochran, 1971; Hermann and Petersen, 1969). These sharp textural breaks introduces large differences in pore sizes, which in turn alter water movement and retention.

Low bulk density ($<0.9 \, g \, cm^{-3}$) is a characteristic feature of Andisols owing to large amounts of SRO minerals and SOM that facilitate creation of porous aggregates. Bulk density of solum horizons across the Tambora soils ($1.1 \pm 0.2 \, g \, cm^{-3}$) was higher than previously reported for Andisols in Indonesia ($0.57–0.87 \, g \, cm^{-3}$; Anda et al., 2016; Anda and Dahlgren, 2020a). Bulk density of Andisols decreases with increasing weathering and concentrations of active Al and Fe, with values decreasing to $< 0.9 \, g \, cm^{-3}$ when allophane contents exceed ~ 5% (Shoji et al., 1993a). Hence, the low contents of SRO minerals and SOM are deemed the primary factors leading to weak soil aggregation, which hinders the development of lower bulk density values. In spite of sandy textures, the high porosity of the pyroclastic materials provide a higher water holding capacity than their counterpart intrusive igneous rocks. For example ash/pumice soils have a substantially higher water content at lower tensions, thereby providing more plant-available water, as compared to basalt-derived soils (Geist and Strickler 1978). We estimate a total porosity of ~ 60% based on the $1.1 \, g \, cm^{-3}$ average bulk density and $2.75 \, g \, cm^{-3}$ particle density for andesitic-basalt. This extensive porosity is expected to provide an excellent balance between aeration and plant-available water holding capacity.

4.4.2. Soil pH

The pH_{H2O} values for all solum horizons were neutral to slightly alkaline (7.1–7.6). Proton consumption by rapid chemical weathering of the young pyroclastic materials is capable of maintaining the pH in a near neutral range, providing an optimum pH range for availability of most plant nutrients. Additionally, inputs of sea spray aerosols provide a continuous replenishment of base cations and alkalinity to maintain a high base saturation and slightly alkaline pH values. Importantly, the near neutral pH values prevent Al toxicity, which often becomes an issue for sensitive plants as pH values drop below 5 (Dahlgren et al., 2004). The strong alkalinity (pH 8.2–9.0) in the C2-C6 layers of SWS15 may be due to ineffective deep leaching due to the sharp textural discontinuity leading to accumulation of some secondary carbonate minerals.

4.4.3. Soil organic matter

Pyroclastic materials contain little organic matter or nitrogen, hence primary succession beginning with nitrogen fixers is a required first step to build up N stocks to support further plant community succession and establishment of integrated biogeochemical cycles (Shoji and Takahashi, 2002). The newly formed soils following the 1815 Mt. Tambora eruption are still in their early stages of soil development; yet nutrient cycling between biota and the SOM pool is well established. Globally, soil organic carbon (SOC) stocks in Andosols are estimated to contain about $25.4 \, kg \, C \, m^{-2}$ in the upper 100 cm (Batjes, 1996), which compare to values from 2.3 to $12.8 \, kg \, C \, m^{-2}$ after 200 years of pedogenesis in this study. Nitrogen stocks in the five profiles ranged from 0.21 to $0.77 \, kg \, m^{-2}$ and the overall C:N ratio ranged from 12 to 29 owing to the contrasting vegetation/land use (C:N ratio): nut trees (29) > food crops (18) > livestock grazing (15). Field observations suggest that grazing short-circuits SOM cycling and contributes to lower C:N ratios as nitrogen is concentrated in the urine/dung returned to the soil system (Dahlgren et al., 1997).

Rates of SOC and SON stock accumulation varied by 4- to 6-fold ($11.4–63.4 \, g \, C \, m^{-2} \, yr^{-1}$ and $1.04–3.81 \, g \, N \, m^{-2} \, yr^{-1}$) across the five Tambora profiles, but fell within the range of C accumulation rates for comparably aged volcanic soils from a global assessment by Zehetner (2010). SOC stocks were also similar in range to previous studies of nearby Indonesian soils from Rakata (Krakatau; $25–44 \, g \, C \, m^{-2} \, yr^{-1}$; 100 years; Hardjowigeno, 1992), Rakata ($44–140 \, g \, C \, m^{-2} \, yr^{-1}$;

110 years; Schlesinger et al., 1998) and Mt. Anak Krakatau (34 g C m^{-2} yr^{-1} in upper 25 cm; <85 years; Fiantis et al., 2019). Zehetner (2010) determined that SOC accumulation rates in Holocene volcanic soils decreased exponentially with increasing soil age: from ~ 50 g C m^{-2} yr^{-1} in the first 50 years to<10 g C m^{-2} yr^{-1} after 1000 years. Vegetation recolonization rate is a key factor regulating SOM accumulation rates. Rapid colonization by blue-green algae (cyanobacteria) (1st year), followed by lichen (2nd year), provided sufficient nitrogen to support establishment of grasses and shrubs (3rd to 4th years) in pyroclastic materials from Mt. Talang (West Sumatra) and Mt Sinabung (North Sumatra) (Fiantis et al., 2016, 2019). Once vegetative inputs of organic carbon to the soil system are established, the SOC accumulation rate will depend on physical and chemical stabilization of these organic inputs from microbial decomposition.

Mechanisms contributing to SOC accumulation in volcanic ash soil include organo-metallic complexes, chemical protection and physical protection (Kögel-Knabner and Amelung, 2021). The weak, fine granular structure dominating the examined Tambora soils provides minimal opportunity for physical protection within soil aggregates. Similarly, the low clay content and low abundance of SRO minerals (allophane, imogolite and ferrihydrite) suggest a low potential for chemical stabilization. We examined Pearson's correlation coefficients (*r*-values) among SOC content and various components from selective dissolution analyses of the modern soil horizons (A and B horizons) of the non-agricultural soils (SWS15/16/17) to elucidate potential stabilization mechanisms. A potential role for metal-humus complexes was indicated by the strong SOC correlations with Al_p (0.81) and Fe_p (0.84). While estimates of allophanic materials were considered negligible in terms of absolute values (<2.3%), the strong correlations between SOC and Al_o (0.91) and Si_o (0.78) suggest a plausible role for a SRO aluminosilicate component contributing to SOC stabilization. The Fe_d fraction, consisting of Fe-humus complexes and Fe (hydr)oxides, was significantly correlated (0.79) with SOC, further suggesting a potential role for SOC stabilization in the form of Fe-humus complexes and organic matter-Fe (hydr)oxide interactions. In contrast, the Fe_o fraction demonstrated no significant correlation with SOC, which we attribute, in part, to the partial dissolution of magnetite/maghemite by the oxalate extraction.

These presumed SOC stabilization mechanisms for Mt. Tambora modern soils are consistent with findings from recent tephra deposits in the tropics from Piton des Neiges (Reunion Island) that showed organomineral complexes as the dominant (82.6%) stabilization mechanisms (Calabi-Floody et al., 2011). Candra et al. (2021) attributes high SOC content in young volcanic soils (1.5–4.3 ka) in Galapagos islands to association of organic matter with SRO minerals. Andesitic mudflows on the flanks of Mt. Shasta (California) (7-, 255-, 616-, and ~ 1200 years old) revealed linear C accumulation rates with soil age over the first 600 years (13.9 g m^{-2} yr^{-1}) that then plateaued (Dickson and Crocker, 1954; Lilienfein et al., 2003). The SOC accumulation over the first 255 years was associated with very low levels of ferrihydrite and allophane, similar to the levels determined in this study. Soil organic C and N pools in the Tambora soils are expected to continue to increase as weathering creates additional active Al/Fe to stabilize SOM pools through formation of metal-humus complexes, sorption to reactive surfaces (e.g., allophanic materials, ferrihydrite) and generation of stable soil aggregates (i.e., physical protection).

4.4.4. Rock-derived nutrients

Periodic additions of pyroclastic deposits rejuvenate soils as fresh mineral inputs enhance chemical weathering and the long-term availability of "rock-derived" nutrients (i.e., a slow release fertilizer) (Dahlgren et al., 1999; Dahlgren et al., 2004; Anda and Sarwani, 2012). Total macro- and micro-elements (expressed in oxide of elements) as measured by XRF (Table 6 and Table 2S). Total content of macroelements Ca, K, Mg and P is high in soil solum, suggesting the high nutrient reserves for crops in a long-term (Table 6). In addition, total content of micro-elements (Mn, Zn and Cu) will not be limiting factors

for various crops (Table S2). All these elements may be released from vesicular trachy-andesite rock owing to their rapid weathering under tropical conditions as shown in Fig. 7.

Phosphorus availability in Andisols is often a primary fertility concern owing to their high P retention from sorption/binding to metal humus complexes and SRO minerals (Shoji et al., 1993a; Takahashi and Dahlgren, 2016). Tambora soils exhibited low-to-moderate P retention (17–43%) due to their low overall concentrations of metal-humus complexes, SRO minerals and clay content. Additionally, rapid release of P by chemical weathering of apatite and volcanic glass provides a continuous release of P during the early stages of pedogenesis (Nanzyo et al., 1997). This high potential for P release by chemical weathering is reflected in the high HCl-extractable P_2O_5 values in solum (1720–2860 mg P_2O_5 kg^{-1}) and C (2170–3050 mg P_2O_5 kg^{-1}) horizons. Bicarbonate-extractable P was generally low (7–40 mg P_2O_5 kg^{-1}) compared to values of 20–45 mg P_2O_5 kg^{-1} reported to achieve maximum yields of common agricultural crops (Bai et al., 2013). The higher bicarbonate-extractable P content in the A horizon of SWS2 is likely due to residual P application since this site is used for agricultural cultivation. Further, the near neutral pH values favor lower P retention as P sorption progressively increases at pH values<7 (Nanzyo et al., 1993). In sum, P amendments may be necessary to support high agricultural yields, but excess P additions are susceptible to leaching due to the lower P retention of these soils.

Highly weathered tropical soils (e.g., Ultisols/Oxisols) often suffer from low inputs of rock derived nutrients as primary minerals are progressively depleted by chemical weathering and intense leaching. Rapid weathering of base-rich parent materials provides a steady renewal of "rock-derived" nutrients for plant growth. For example, the high HCl-extractable K_2O values in the solum (580 to 3110 mg K_2O kg^{-1}) were similar to the concentrations in the minimally-weathered C horizons (1020–2060 mg K_2O kg^{-1}) of SWS2 and SWS15 reflecting the K-rich nature of the trachyandesite. Given the proximity of the sites to the ocean, there is also continuous deposition of important nutrients, such as Ca^{2+}, Mg^{2+}, K^+ and SO_4^{2-}, from wet and dry deposition of sea salts. The inputs of nutrients from chemical weathering and sea salts are very important as cation nutrient retention (CEC) is low due to the low clay contents. Surface horizons enriched in SOM have appreciably higher CEC values to store nutrient cations for plant utilization. Thus, nutrient retention by CEC and nutrient release from organic matter will continue to increase as organic matter stocks and clay contents increase with progressive soil development.

5. Conclusions

Soil development in the 1815 pyroclastic deposits from Mt. Tambora eruption has resulted in the development of A and Bw horizons with total solum depths of 25 to 107 cm. Soil mineralogical composition of the sand fraction was dominated by easily weatherable minerals consisting of labradorite, augite and volcanic glass with little sanidine and biotite. Minerals more resistant to weathering consisted of opaque minerals (2–39%) and very scarce quartz (<1%). The dominance of weatherable minerals has a positive impact on many soil nutrient reserves for agricultural crops (e.g., Ca, Mg, K, P). Formation of allophanic materials was minimal (<2.3%), possibly owing to the preferential accumulation of Al^{3+} in Al-humic complexes as organic matter stocks rapidly increased over the 200 year period. Measures of chemical weathering (e.g., chemical index of alteration (CIA) and base depletion index (BDI)) indicated a pattern of increasing accumulation of Al oxides and depletion of base cations (Ca^{2+}, Mg^{2+}, K^+, Na^+) at the soil surface relative to the C horizons and unweathered rocks. Based on the solum (A + B horizons) depths (25 to 107 cm) and 200 years of post-eruption soil development, the soil formation rate ranged from 1.2 to 5.3 mm yr^{-1}.

The bulk density of solum horizons across the investigated soils (1.1 ± 0.2 g cm^{-3}) was similar to C horizon materials as a result of weak
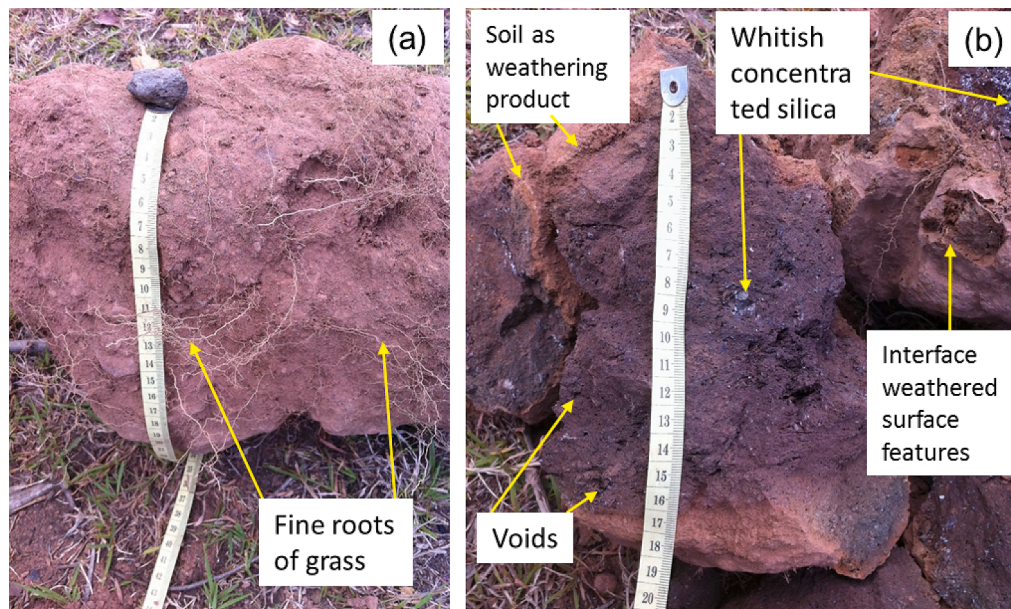
Fig. 7. Weathering of vesicular trachyandesite rock collected at 50 cm from the soil surface showing its alteration to 200 years after the Tambora eruption, as represented by the SWS17 profile: (a) trachyandesite covered by its soil weathering products and many fine roots of grasses, and (b) closeup of the exposed internal fresh surface of figure (a), showing many vesicular voids, whitish silica deposits, interface weathered surface features of trachyandesite, and the weathered soil.

soil structure development owing to low SOC and SRO mineral concentrations that serve as soil particle binding agents. Phosphate retention was relatively low (17.5–43.4%) within the soil solum owing to low allophane content and near-neutral soil pH values. Rapid weathering of the glassy parent materials resulted in a neutral to slightly alkaline soil pH range as silicate weathering consumes protons and simultaneously releases an abundance of rock-derived nutrients. SOC (2.3–12.8 kg C m^{-2}) and SON (0.21 to 0.77 kg m^{-2}) stocks accumulated at rates comparable to similarly aged volcanic soils beginning with primary succession in newly deposited pyroclastic materials. SOC stabilization by the formation of metal-humus complexes was suggested by strong relationships between Al_p and Fe_p with SOC. Overall, rapid soil development over the 200-year time period has resulted in moderately productive agricultural soils with integrated nutrient cycles. It is expected that the agricultural potential of these soils will continue to increase in the short-term (the next few thousand years) as organic matter and clay contents increase with progressive soil development, thereby providing increased nutrient and water storage capacities.

Declaration of Competing Interest

The authors declare that they have no known competing financial interests or personal relationships that could have appeared to influence the work reported in this paper.

Data availability

Data will be made available on request.

Acknowledgments

Appendix A. Supplementary data

Supplementary data to this article can be found online at https://doi.org/10.1016/j.geoderma.2023.116454.

References

Abrams, L.J., Sigurdsson, H., 2007. Characterization of pyroclastic fall and flow deposits from the 1815 eruption of Tambora volcano, Indonesia using ground-penetrating radar. J. Volcanol. Geoth. Res. 161, 352–361.
Algoe, C., Stoops, G., Vandenberghe, R.E., Van Ranst, E., 2012. Selective dissolution of Fe-Ti oxides – extractable iron as a criterion for andic properties revisited. Catena 92, 49–54.
Anda, M., Dahlgren, R.A., 2020a. Long-term response of tropical Andisol properties to conversion from rainforest to agriculture. Catena 194, 104679.
Anda, M., Dahlgren, R.A., 2020b. Mineralogical and surface charge characteristics of Andosols experiencing long-term, land-use change in West Java. Indonesia. Soil Sci. Plant Nutr. 66, 702–713.
Anda, M., Sarwani, M., 2012. Mineralogy, chemical composition, and dissolution of fresh ash eruption: New potential source of nutrients. Soil Sci. Soc. Am. J. 76, 733–747.
Anda, M., Suparto, Sukarman, 2016. Characteristics of pristine volcanic materials: Beneficial and harmful effects and their management for restoration of agroecosystem. Sci. Total Environ. 543, 480–492.
Bai, Z., Li, H., Yang, X., Zhou, B., Shi, X., Wang, B., Li, D., Shen, J., Chen, Q., Qin, W., Oenema, O., Zhang, F., 2013. The critical soil P levels for crop yield, soil fertility and environmental safety in different soil types. Plant Soil 372, 27–39.
Batjes, N.H., 1996. Total carbon and nitrogen in the soils of the world. Eur. J. Soil Sci. 47, 151–163.
Blakemore, L.C., Searle, R.L., Daly, B.K., 1987. Methods for Chemical Analysis of Soils. New Zealand Soil Bureau Science. Report 80. New Zealand Society of Soil Science. Lower Hutt.
Bockheim, J.G., 1980. Solution and use of chronofunctions in studying soil development. Geoderma 24, 71–85.
Bremner, M., Mulvaney, C.S., 1982. Nitrogen-total, In: Page, A.L., Miller, R.H., Keeny, D. R. (Eds.), Methods of Soil Analysis, Part 2. Chemical and Mineralogical Properties, Monograph No. 9. Agronomy Series No. 9. 2nd ed. ASA and SSSA, Madison, WI, pp. 595–624.
Calabi-Floody, M., Bendall, J.S., Jara, A.A., Welland, M.E., Theng, B.K., Rumpel, C., de la Luz Mora, M., 2011. Nanoclays from an Andisol: Extraction, properties and carbon stabilization. Geoderma 161, 159–167.
Candra, I.N., Gerzabek, M.H., Ottner, F., Wriessnig, K., Tintner, J., Schmidt, G., Rechberger, M.V., Rampazzo, N., Zehetner, F., 2021. Soil development and mineral transformations along a one-million-year chronosequence on the Galapagos Islands. Soil Sci. Soc. Am. J. 85, 2077–2099.
Chartres, C.J., Van Reuler, H., 1985. Mineralogical changes with depth in a layered Andosol near Bandung, Java (Indonesia). J. Soil Sci. 36, 173–186.
Cochran, P. H., 1971. Pumice particle bridging and nutrient levels affect lodgepole and ponderosa pine seedling development. Res. Note PNW-150. Portland, OR: U.S.

Department of Agriculture, Forest Service, Pacific Northwest Forest and Range Experiment Station. 10 p.

Dahlgren, R., 1994. Quantification of Allophane and Imogolite. In: Amonette, J.E., Stucki, J.W. (Eds.), Quantitative Methods in Soil Mineralogy. Soil Science of America Inc, Madison, WI, USA, pp. 430–451.

Dahlgren, R.A., Ugolini, F.C., 1990. The effects of tephra perturbations on soil processes in a tephritic Spodosol, Cascade Range, Washington. Geoderma 45, 331–355.

Dahlgren, R.A., Singer, M.L., Huang, X., 1997. Oak tree and grazing impacts on soil properties and nutrients in a California oak woodland. Biogeochemistry 39, 45–64.

Dahlgren, R.A., Ugolini, F.C., Casey, W.H., 1999. Field weathering rates of Mt. St. Helens tephra. Geochim. Cosmochim. Acta. 63, 587–598.

Dahlgren, R.A., Saigusa, M., Ugolini, F.C., 2004. The nature, properties and management of volcanic soils. Adv. Agron. 82, 113–182.

Dickson, B.A., Crocker, R.L., 1953. A chronosequence of soils and vegetation near Mt. Shasta, California: II. The development of the forest floor and the carbon and nitrogen profiles of the soils. J. Soil Sci. 4, 142–156.

Dickson, B.A., Crocker, R.L., 1954. A chronosequence of soils and vegetation near Mt. Shasta, California: III. Some properties of the mineral soils. J. Soil Sci. 5, 173–191.

Fiantis, D., Nelson, M., Shamshuddin, J., Goh, T.B., Ranst, E.V., 2016. Initial carbon storage in new tephra layers of Mt. Talang in Sumatra as affected by pioneer plants. Commun. Soil Sci. Plant Anal. 47, 1792–1812.

Fiantis, D., Ginting, F.I., Gusnidar, Nelson, M., Minasny, B., 2019. Volcanic ash, insecurity for the people but securing fertile soil for the future. Sustainability 11, 3072. https://doi.org/10.3390/su11113072.

Fick, S.E., Hijmans, R.J., 2017. WorldClim 2: new 1-km spatial resolution climate surfaces for global land areas. Int. J. Climatol. 37, 4302–4315.

Garcıa-Rodeja, E., Novoa, J.C., Pontevedra, X., Martinez-Cortizasa, A., Buurman, P., 2004. Aluminium fractionation of European volcanic soils by selective dissolution techniques. Catena 56, 155–183.

Geist, J. M., Strickler, G. S., 1978. Physical and chemical properties of some Blue Mountain soils in northeast Oregon. Res. Pap. PNW-236. Portland, OR: U.S. Department of Agriculture, Forest Service, Pacific Northwest Forest and Range Experiment Station. 19 p.

Gertisser, R., Self, S., 2015. The great 1815 eruption of Tambora and future risks from large-scale volcanism. Geol. Today 31, 132–136.

Hardjowigeno, S., 1992. The development and nature of soils on Rakata. GeoJournal 28, 131–138.

Harnois, L., 1988. The CIW index: a chemical index of weathering. Sed. Geol. 55, 319–322.

Hermann, R., Petersen, R.G., 1969. Root development and height increment of ponderosa pines in pumice soils of central Oregon. For. Sci. 15, 226–237.

Higashi, T., 1983. Characterization of Al/Fe–humus complexes in Dystrandepts through comparison with synthetic forms. Geoderma 31, 277–288.

Holmgren, G.G., 1967. A rapid citrate-dithionite extractable iron procedure. Soil Sci. Soc. Am. Proc. 31, 210–211.

Inoue, K., Higashi, T., 1988. Al– and Fe–humus complexes in Andisols. In "Proceedings 9th Int. Soil Classification Workshop, Japan" (D. I. Kinloch, S. Shoji, F. M. Beinroth, and H. Eswaran, Eds.), pp. 535–546. Japanese Committee for 9th International Soil Classification Workshop and Soil Management Support Services, Washington, D.C.

Jien, S.H., Baillie, I., Huang, I.W., Chen, Y.Y., Chiu, C.Y., 2016. Incipient ferralization and weathering indices along a soil chronosequence in Taiwan. Eur. J. Soil Sci. 67, 583–596.

Kögel-Knabner, I., Amelung, W., 2021. Soil organic matter in major pedogenic soil groups. Geoderma 384, 114785.

Lilienfein, J., Qualls, R., Uselman, S.M., Bridgham, S., 2003. Soil formation and organic matter accretion in a young andesitic chronosequence at Mt. Shasta, California. Geoderma 116, 249–264.

Lyu, H., Watanabe, T., Kilasara, M., Funakawa, S., 2018. Effects of climate on distribution of soil secondary minerals in volcanic regions of Tanzania. Catena 166, 209–219.

Lyu, H., Watanabe, T., Ota, Y., Nakao, A., Hartono, A., Anda, M., Dahlgren, R., Funakawa, S., 2022. Climatic controls on soil clay mineral distributions in humid volcanic regions of Sumatra and Java, Indonesia. Geoderma 425, 116058.

Milner, H.B., 1962. Sedimentary Petrography: With Special Reference to Petrographic Methods of Correlation of Strata, Petroleum Technology and Other Economic Applications of Geology. Publisher G. Allen and Unwin, London.

Nanzyo M, Dahlgren R, and Shoji S 1993. Chemical characteristics of volcanic ash soils. In: Volcanic Ash Soils - Genesis, Properties and Utilization. Dev. Soil Sci. (Amsterdam: Elsevier) pp 145-187.

Nanzyo, M., Takahashi, T., Sato, A., Shoji, S., Yamada, I., 1997. Dilute acid-soluble phosphorus in fresh air-borne tephras and fixation with an increase in active aluminum and iron. Soil Sci. Plant Nutr. 43, 839–848.

Nesbitt, H.W., Young, G., 1982. Early Proterozoic climates and plate motions inferred from major element chemistry of lutites. Nature 299, 715–717.

Nesbitt, H.W., Young, G.M., 1989. Formation and diagenesis of weathering profiles. J. Geol. 97, 129–147.

Norrish, K., Chappell, B.W., 1977. X-ray fluorescence spectrography. In: Zussmann, J. (Ed.), Physical Methods in Determinative Mineralogy. Academic Press, London, pp. 201–272.

Olsen, S.R., 1954. Estimation of available phosphorus in soils by extraction with sodium bicarbonate. United States Department of Agriculture, Washington DC.

Parfitt, R.L., 1990. Allophane in New Zealand-A Review. Aust. J. Soil Res. 28, 343–360.

Parfitt, R.L., 2009. Allophane and imogolite: In soil biogeochemical processes. Clay Miner. 44, 135–155.

Parfitt, R.L., Childs, C.W., 1988. Estimation of forms of Fe and Al: a review, and analysis of contrasting soils by dissolution and Mossbauer methods. Aust. J. Soil Res. 26, 121–144.

Parfitt, R.L., Kimble, J.M., 1989. Conditions for Formation of Allophane in Soils. Soil Sci. Soc. Am. J. 53, 971–977.

Rasmussen, C., Matsuyama, N., Dahlgren, R.A., Southard, R.J., Brauer, N., 2007. Soil genesis and mineral transformation across an environmental gradient on andesitic lahar. Soil Sci. Soc. Am. J. 71, 225–237.

Rennert, T., 2019. Wet-chemical extractions to characterise pedogenic Al and Fe species – a critical review. Soil Res. 57, 1–16.

Schlesinger, W.H., Bruijnzeel, L., Bush, M.B., Klein, E.M., Mace, K.A., Raikes, J.A., Whittaker, R., 1998. The biogeochemistry of phosphorus after the first century of soil development on Rakata Island, Krakatau, Indonesia. Biogeochemistry 40, 37–55.

Schwertmann, U., 1985. The Effect of Pedogenic Environments on Iron Oxide Minerals. In: Stewart, B.A. (Ed.), Advances in Soil Science. Springer, New York, New York, NY, pp. 171–200.

Self, S., Rampino, M.R., Newton, M.S., Wolff, J.A., 1984. Volcanological study of the great Tambora eruption of 1815. Geology 12, 659–663.

Self, S., Gertisser, R., Thordarson, T., Rampino, M.R., Wolff, J.A., 2004. Magma volume, volatile emissions, and stratospheric aerosols from the 1815 eruption of Tambora. Geophys. Res. Lett. 31, L20608.

Shoji, S., Nanzyo, M., Dahlgren, R.A., 1993a. Volcanic Ash Soils—Genesis, Properties and Utilization, 288. Elsevier, Amsterdam, the Netherlands.

Shoji, S., Nanzyo, M., Shirato, Y., Ito, T., 1993b. Chemical kinetics of weathering in young Andisols from northeastern Japan using soil age normalized to 10°C. Soil Sci. 155, 53–60.

Shoji, S., Takahashi, T., 2002. Environmental and agricultural significance of volcanic ash soils. Glob. Environ. Res. 6, 113–135.

Sigurdsson, H., Carey, S., 1989. Plinian and co-ignimbrite tephra fall from the 1815 eruption of Tambora volcano. Bull. Volcanol. 51, 243–270.

Sigurdsson, H., Carey, S., 1992. Eruptive history of Tambora volcano, Indonesia. Mitteilungen aus dem Geologisch-Pala. "ontologischen Institut der Universita" t Hamburg 70, 187–206.

Soil Survey Staff, 1992. Soil Survey Laboratory Methods Manual. Soil Survey Investigations Report No. 42, USDA-SCS, Washington DC.

Soil Survey Staff, 2014. Kellogg soil survey laboratory methods manual. Soil Survey Investigations Report No. 42, Version 5.0. U.S. Department of Agriculture, Natural Resources Conservation Service, Washington DC.

Sollins, P., Spycher, G., Topik, C., 1983. Processes of soil organic matter accretion at a mudflow chronosequence, Mt. Shasta, California. Ecology 64, 1273–1282.

Stockmann, U., Minasny, B., McBratney, A., 2014. How fast does soil grow? Geoderma 216, 48–61.

Stommel, H.M., Stommel, E., 1979. The year without a summer. Sci. Am. 240, 176–186.

Stothers, R.B., 1984. The Great Tambora eruption in 1815 and its aftermath. Science 224, 1191–1198.

Sudradjat, A., Mangga, S.A., Suwarna, N., 1998. Geological map of the Sumbawa quadrangle. Nusa Tenggara. Geological Research and Development Centre, Bandung, Indonesia.

Takahashi, T., Dahlgren, R.A., 2016. Nature, properties and function of aluminum-humus complexes in volcanic soils. Geoderma 263, 110–121.

Takahashi, T., Dahlgren, R.A., van Susteren, P., 1993. Clay mineralogy and chemistry of soils formed in volcanic materials in the xeric moisture regime of northern California. Geoderma 59, 131–150.

Talibudeen, O., 1981. Precipitation. In: Greenland, D.J., Hayes, M.H.B. (Eds.), The Chemistry of Soil Processes. John Wiley & Sons, New York, pp. 81–114.

Torrent, J., Schwerrmann, U., Fechrer, H., Averez, F., 1983. Quantitative relationships between soil color and hematite content. Soil Sci. 136, 354–358.

van Oosterzee, P., 1997. Where worlds collide: the Wallace Line. Cornell University Press, Ithaca.

Van Ranst, E., Utami, S.R., Shamshuddin, J., 2002. Andisols on volcanic ash from Java Island. Indonesia: physico-chemical properties and classification. Soil Sci. 167, 68–79.

Wada, K., 1985. The distinctive properties of Andosols. Adv. Soil Sci. 2, 173–229.

Wada, K., 1986. Ando Soils in Japan. Kyushu University Press, Fukuoka, Japan. p. 276.

Wakatsuki, T., Rasyidin, A., 1992. Rates of weathering and soil formation. Geoderma 52, 251–263.

Wolff-Boenisch, D., Gislason, S.R., Oelkers, E.H., Putnis, C.V., 2004. The dissolution rates of natural glasses as a function of their composition at pH 4 and 10.6, and temperatures from 25 to 74°C. Geochim. Cosmochim. Acta 68, 4843–4858.

Yokoyama, I., 1957. Energetics in active volcanoes. Tokyo Univ. Earthq. Res. Inst. Bull. 35, 75–97.

Zehetner, F., 2010. Does organic carbon sequestration in volcanic soils offset volcanic CO2 emissions? Quat. Sci. Rev. 29, 1313–1316.